SBUF

PROJECTNR. 14488

Evaluation of Alternative Particle Size Distributions for Railway Ballast

Utvärdering av alternativa storleksfördelningar för järnvägsmakadam

Johannes Quist, Pontus Malmsköld, Anita Ullrich, Caroline Ansin
Fraunhofer-Chalmers Centre
Kristoffer Hofling
NCC Industry

Andreas Persson, Christoffer Brauer, Mikael Knutsson
Dynapac Compaction Equipment

Magnus Evertsson
Chalmers University of Technology

2026-04-30

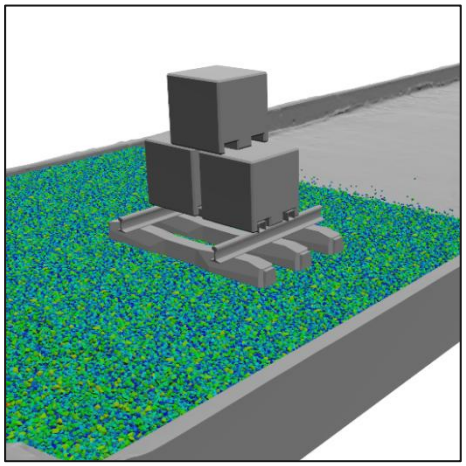

Preface

This report presents the results from the SBUF project on evaluation of alternative particle size distributions for railway ballast. The work has been carried out as a collaborative effort between Fraunhofer-Chalmers Centre, NCC Industry, Dynapac Compaction Equipment, and Chalmers University of Technology, combining experimental testing and numerical modelling to assess the influence of particle size distribution on ballast behaviour.

The main author of this report is Johannes Quist, with contributions from Pontus Malmsköld, Caroline Ansin and Kristoffer Hofling.

The authors would like to express their sincere appreciation to all partners and individuals who have contributed to the project. In particular, the team at Dynapac Compaction Equipment (Andreas Persson, Christoffer Brauer, Mikael Knutsson, and Maria Wilhelmsson) is gratefully acknowledged for their extensive work on the development of the sleeper push test setup, including rig design, construction, and dedicated efforts during the testing campaigns. Special thanks are also extended to Per Olsson (POAB) for excellent work with excavation and machinery operations, and for his practical expertise during the test execution.

The authors would further like to thank Alex Hägerström at NCC Hemmesjö for support with ballast production and handling of the specially prepared materials, as well as Urban Svensson at Walleverken for providing the hydraulic system used in the test setup. A special acknowledgement is directed to Heidelberg Materials Abetong and Ulf Malmqvist for generously supplying sleepers and fastening systems to the project.

Finally, the authors would like to thank the project reference group for valuable input and discussions throughout the project, including Jan Englund and Joel Björkquist (Skanska), Peter Martinsson (Swerock), Magnus Evertsson (Chalmers University of Technology), Klas Hermelin and Johan Jonsson (Trafikverket), and Björn Schouenborg and Lars Jacobsson (RISE).

The project has been financed by SBUF and Vinnova InfraSweden2030, whose support is gratefully acknowledged.

April 2026

Johannes Quist

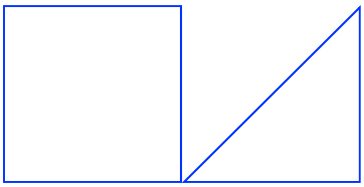

Sammanfattning (Svenska)

Bakgrund och problemformulering

Järnvägsmakadamens funktion påverkas i hög grad av dess storleksfördelning, som styr packning, lastöverföring, deformation och nedbrytning. Nuvarande standard tillåter variation inom givna spann, men det saknas fortfarande en tydlig förståelse för hur alternativa fördelningar påverkar mekaniskt beteende, degradering och långsiktig funktion i spår.

Syfte med projektet

Syftet med projektet är att utvärdera hur olika storleksfördelningar påverkar järnvägsmakadams mekaniska respons och fragmenteringsbeteende, samt att etablera en grund för vidare studier av mer optimerade materialfördelningar.

Kort beskrivning av metod

Studien bygger på en kombination av experimentella och numeriska metoder:

- Storskaliga sleeper push tester för att studera skjuvbeteende och sidomotstånd
- Cykliska oedometerförsök för deformation, styvhetsutveckling och nedbrytning
- Standardiserade ballasttester enligt SS-EN
- DEM-simuleringar (Demify) för analys av partikelinteraktioner och kraftöverföring

Tre material studerades: standardfördelning (M1), bredare fördelning (M2) samt en bimodal fördelning (M3/M3.2).

Viktigaste resultat

- Storleksfördelningen har en tydlig påverkan på både deformation och fragmentering
- M1 uppvisar störst permanent deformation och högst grad av nedbrytning
- M2 och M3/M3.2 uppvisar lägre total fragmentering
- Den bimodala fördelningen ger relativt hög finmaterialgenerering trots lägre total nedbrytning
- Inspänning och lastnivå har större påverkan på skjuvrespons än skillnader i storleksfördelning
- DEM-simuleringarna återger huvudsakliga trender i experimenten och ger en mekanistisk förklaring baserad på kraftfördelning mellan partiklar

Begränsningar

- Skalning av storleksfördelningar i oedometerförsöken
- Avsaknad av partikelkrossning i DEM-modellen
- Begränsat antal material och testfall
- Förenklade randvillkor och initialt packningstillstånd i simuleringarna

Fortsatt arbete och utvecklingsmöjligheter

Resultaten visar att den använda metodiken utgör en grund för en mer systematisk analys av ballastens storleksfördelning. Den etablerade experimentella och numeriska plattformen möjliggör vidare studier där ett bredare spann av fördelningar och partikelegenskaper kan analyseras. Detta inkluderar även koppling till mer representativa testförhållanden, utökade experimentella uppställningar och vidareutveckling av DEM-modellerna för att bättre beskriva nedbrytning och långtidsegenskaper.

Summary

This study evaluates the influence of particle size distribution (PSD) on the mechanical behaviour and degradation of railway ballast. Three materials were investigated: a standard class I ballast (M1), a broader grading (M2), and a bi-modal distribution (M3/M3.2).

The project combines large-scale experimental testing with numerical simulations using the Discrete Element Method (DEM). The experimental program includes a newly developed sleeper push test to assess lateral resistance and shear behaviour, as well as cyclic oedometer tests to evaluate deformation, stiffness evolution, and particle breakage. Standard ballast tests were also performed according to relevant European standards.

The results show that particle size distribution has a clear influence on both deformation behaviour and fragmentation. The standard ballast (M1) exhibits the largest permanent deformation and the highest degree of breakage and redistribution of material. The broader and bi-modal gradings show reduced overall breakage, although the bi-modal material demonstrates relatively high fines generation, indicating a different fragmentation mechanism.

In the sleeper push tests, vertical load and confinement conditions strongly influence the mobilized resistance. Increased confinement primarily leads to higher apparent cohesion, while the friction angle remains relatively insensitive to PSD variations. Differences between the investigated gradings are observable but secondary compared to the influence of boundary conditions.

The DEM simulations, performed using the Demify software, reproduce the main qualitative trends observed in the experiments, including force–displacement behaviour and the relative differences in deformation and stiffness between materials. The simulations also provide insight into particle-scale mechanisms, showing how differences in force distribution and load transfer may explain the observed macroscopic response. Quantitative deviations remain, primarily due to simplifications such as the absence of particle breakage and idealized initial packing conditions.

The study demonstrates that PSD is a relevant parameter influencing both mechanical performance and degradation behaviour of railway ballast. The combined experimental and numerical framework established in this work provides a basis for further, more systematic evaluation of ballast gradings, including extended test conditions and a broader range of particle size and shape distributions in relation to performance, durability, and production considerations.

1 Content

Background

Railway ballast, its properties, and its in-service behavior are central to the performance and expected service life of ballasted railway superstructures. The ballast layer transfers loads from the train, through the rails and sleepers, to the underlying layers. The material must therefore satisfy several partly competing requirements related to strength, frost resistance, abrasion resistance, stability, stiffness, and drainage. In addition, railway ballast has to be produced, transported, and handled efficiently from a suitable quarry and then placed correctly beneath and around the sleepers in the track structure.(Göransson, 2018; SIS, 2003).

Viewed as a particulate system, ballast performance depends both on the properties of the individual particles and on the grading of the aggregate skeleton as a whole. Particle shape, mineralogical composition, resistance to fragmentation, and resistance to wear are important, but the particle size distribution also governs how the ballast packs, how interparticle contacts are mobilized, how stresses are redistributed through the skeleton, and how the material dilates, settles, and breaks under repeated loading. In other words, ballast performance cannot be understood from rock quality alone; it must be considered as a coupled material-and-structure problem at particle, layer, and track levels (Indraratna B. et al., 1998; Indraratna et al., 2016; Rosa et al., 2021).

Within the Swedish specification framework, class-I railway ballast is nominally defined as 31.5/63 mm. However, the standards do not prescribe one unique grading curve. SS-EN 13450 (SIS, 2003) provides the product-standard framework, while TRVINFRA-00019 states that class-I ballast shall belong to either grading category E or grading category F. Category E is the broader envelope, with a larger allowance of particles between 22.4 and 31.5 mm, whereas category F is narrower (Trafikverket, 2020). This is an important nuance: the Swedish system already allows some flexibility in grading within the nominal 31.5/63 fraction, which means that the present “standard” is not a single sharply fixed curve but a bounded specification window. (SS-EN 13450:2003; TDOK 2014:0759; Göransson, 2018)

Despite long-established specification practice, ballast degradation, ballast fouling, differential settlement, and stiffness variations remain major causes of reduced track performance and increased maintenance demand. Ballast and sub-ballast degrade through particle reorientation, wear, and fouling, while abrupt stiffness variations at transitions, switches, crossings, insulated joints, and hanging sleepers amplify wheel–rail contact forces and accelerate settlement and geometry deterioration. Swedish experience reported in the bearing-capacity literature further shows that deficient support conditions manifest themselves as recurring geometry defects and increased maintenance needs in both the track and the drainage system. (Berggren, 2009; Dehlbom et al., 2018)

There are therefore strong technical and economic reasons to examine whether alternative ballast gradings can provide a better balance between stability, drainage, deformation resistance, and long-term durability than present practice. The issue is also relevant from a production perspective, since a broader grading may improve

product yield from a given crushing process, and from a maintenance perspective, since ballast is in an especially vulnerable and relatively loose state immediately after construction or corrective maintenance, before traffic has recompacted the granular skeleton. These aspects are particularly important in locations with repeated geometry correction, such as transition zones and switches, where the combined effects of repeated maintenance and rapidly varying support conditions can accelerate degradation. (Berggren, 2009; Indraratna B. et al., 1998; Lundqvist & Dahlberg, 2005)

1.1 Current state of research on ballast particle size distribution

The literature does not support a simple rule stating that either a narrower or a broader grading is always superior. Instead, ballast behavior emerges from the interaction between grading, particle shape, lithology, density, confining pressure, loading frequency, and loading history. This is one of the most important overall conclusions to draw from the available material: “optimal” grading is conditional on what performance criterion is prioritized and under which test and loading conditions that criterion is evaluated. (Indraratna B. et al., 1998; Indraratna et al., 2016; Rosa et al., 2021)

Large-scale triaxial testing by Indraratna, Ionescu and Christie showed that ballast behavior at low confining pressure differs markedly from behavior at higher confining pressure, which is highly relevant for real track conditions where the effective confining stress in ballast is relatively low. In their study, shear strength and particle crushing were mainly influenced by particle size distribution, grain angularity, and initial density. They also emphasized the importance of compaction in the crib and shoulders, because confinement strongly affects dilation, breakage, and overall ballast response. Their conclusion was not that grading alone governs performance, but that grading has to be interpreted together with packing state and confinement. (Indraratna B. et al., 1998)

Under cyclic loading, Indraratna, Sun and Nimbalkar (2016) found a distinctly non-monotonic grading effect. In their large-scale cyclic triaxial tests, larger ballast aggregates experienced smaller axial and radial strains, while resistance to plastic strain improved with increasing relative density. At the same time, permanent axial strain and volumetric strain first decreased and then increased as the coefficient of uniformity, Cu, increased. They also identified two breakage regimes: a high-breakage zone for lower Cu values and a reduced-breakage zone when Cu exceeded approximately 1.8. Based on these tests, they proposed an optimum ballast grading corresponding to Cu in the range of about 1.8–2.0, with associated grading descriptors λ = 3.0–4.4 and E = 0.375–0.376 in their notation. Their study is especially important because it argues not for the broadest possible grading, but for an intermediate grading that balances deformation and degradation under high-frequency cyclic loading. (Indraratna, Sun & Nimbalkar, 2016.)

Rosa, Aragão and Motta (2021) widened the discussion by showing that lithology and morphology can modify the grading effect substantially. In their scaled triaxial study, the particle size distribution directly affected ballast behavior, but the response also depended on the rock type and the morphology of the particles. They observed a good correlation between fines generation, lithology, and coefficient of uniformity, and they showed that, under their test conditions, the percentages passing 4.75 mm and 2 mm

were more informative indicators of breakage than some of the more traditional aggregate breakage indices. Their DEM-supported analysis further indicated that as packing became denser, the total number of particles and contacts increased, whereas the coordination number decreased; they also concluded that the coordination number was inversely proportional to breakage potential. Importantly, they noted that Cu alone could not distinguish all observed PSD behaviors, which means that grading width by itself is not a sufficient descriptor of ballast performance. (Rosa, Aragão & Motta, 2021.)

At superstructure level, the grading issue is inseparable from track stiffness and the distribution of support conditions along the track. Berggren showed that track stiffness affects bearing capacity, wheel–rail interaction, track geometry quality, and the service life of track components. He also pointed out that both very low and very high stiffness can be problematic: low stiffness increases rail deflections and bending moments, whereas very high stiffness increases dynamic forces on sleepers and ballast. Dahlberg, in turn, demonstrated how abrupt stiffness changes at transitions, bridges, switches, and similar locations intensify wheel–rail force variation and thereby accelerate settlement, fatigue, and local deterioration. From this perspective, ballast grading matters not only because it influences particle breakage, but also because it contributes to overall track support characteristics and the severity of differential settlement. (Berggren, 2009; Lundqvist & Dahlberg, 2005)

Taken together, the present state of research suggests that ballast particle size distribution influences railway performance through at least four coupled mechanisms: packing and interlock, drainage and fines accommodation, contact-force distribution and breakage, and the stiffness/settlement behavior of the track support system. Any technically defensible assessment of alternative gradings must therefore examine both ballast durability and system-level performance.

1.2 Standards and Swedish practice

The Swedish specification system makes a clear functional distinction between the coarse upper ballast layer and the more broadly graded underballast layers below it. Göransson's overview describes the upper ballast as a coarse crushed rock material, normally in the size range 31.5–63 mm, whose role is to provide load transfer, drainage, frictional stability, and sufficient elasticity in the sleeper–ballast system. The underballast (sub-ballast), by contrast, is much more broadly graded, typically around 0/150 mm, and is intended to distribute traffic loads, ensure drainage of the track bed, protect the formation against erosion, and mitigate settlement and frost effects. This layered logic is consistent with AMA Anläggning, where well graded underballast materials are prescribed for reinforcement and frost insulation. (Göransson, 2018; AMA Anläggning 20, DCH.15–DCH.16.)

In the current Trafikverket specification (Trafikverket, 2020), this distinction is formalized through strict requirements on ballast geometry, shape, and fines content. For class I ballast, the nominal size class remains 31.5/63 mm, with very low allowable fines content (≤ 0.5%) and explicit requirements on particle angularity through the LT index, reflecting the need for a coarse, open, and highly interlocked structure. At the same time, the specification allows two grading categories, E and F, within this size

class. Category E permits a broader grading with a larger proportion of particles in the intermediate size range (e.g. up to 25% passing 31.5 mm), whereas category F is more narrowly graded with stricter limits on intermediate fractions.

This distinction between E and F grading categories was already present in TDOK 2014:0759 (Trafikverket, 2015) and has been carried forward into the current specification. It is technically significant because it shows that the Swedish standard does not prescribe a single grading, but instead defines an allowable design space within the same nominal ballast product. In other words, both relatively narrow and relatively broad gradings are considered acceptable, provided that they meet the functional requirements on drainage, mechanical stability, and durability.

Read together, SS-EN 13450 and the Trafikverket specification function primarily as a product quality and conformance framework rather than a mechanistic design rule. The standard defines test methods, acceptance limits, and categories, while leaving it to the purchaser and designer to select appropriate properties for a given application. The coexistence of both E and F grading categories within class I ballast reinforces that there is no universally optimal grading independent of loading conditions, substructure, climate, and maintenance strategy.

A reasonable inference from the Swedish layered specification system is that it intentionally separates the functions of the open, drainage oriented ballast layer from the more broadly graded load distributing layers below. This has direct implications for the present project. If the upper ballast grading is broadened excessively, the functional distinction between ballast and underballast may begin to blur, particularly with respect to drainage capacity, tamping behavior, and fines migration. Conversely, if the grading is too narrow, contact stresses and local particle breakage may increase, especially under cyclic loading. The practical design space is therefore bounded not only by particle scale mechanics, but also by how the specification framework allocates different functions to different layers in the track system. This is precisely why the question of optimal ballast grading remains open despite long standing standards.

1.3 Tensions in the literature

The first clear tension concerns whether a broader grading is beneficial or detrimental. On the one hand, the cyclic-ballast literature summarized by Indraratna, Sun and Nimbalkar notes that a more broadly graded PSD has often been suggested to improve interlock. On the other hand, the earlier large-scale work by Indraratna, Ionescu and Christie concluded that ballast with a broader gradation and dense compaction could undergo greater degradation upon loading. The later cyclic study then refined the picture further by showing that the relationship is non-monotonic: breakage is high at low Cu, reduced above about Cu = 1.8, but deformation does not continue to improve indefinitely with increasing grading width. The practical implication is that “broader” is not a sufficient design principle; the question is how broad, under what density, and for which loading regime. (Indraratna, Ionescu & Christie, 1998; Indraratna, Sun & Nimbalkar, 2016.)

The second tension concerns whether grading can be treated as the dominant variable. Swedish standards and application practice naturally put considerable emphasis on grading windows, nominal fractions, and category compliance. However, Rosa, Aragão and Motta show that lithology and morphology can shift the degradation response substantially, and that Cu alone could not explain all the observed PSD behaviors in their study. In other words, a grading that performs well in one rock type may not perform equally well in another, even if the sieve curve is nominally similar. This means that a standards-based view of grading must be complemented by a material-specific view of breakage resistance and particle shape. (Rosa, Aragão & Motta, 2021; Göransson, 2018.)

The third tension concerns scale and method. Rosa, Aragão and Motta explicitly note that scale reduction of ballast for small-scale testing is not fully consensual in the literature, because smaller particles may require different specific breakage energy and may not reproduce field-scale fracture mechanisms exactly. By contrast, the two Indraratna studies cited here rely on large-scale triaxial testing and are therefore closer to field particle sizes. The literature is therefore internally consistent in one important respect: it repeatedly shows that conclusions about grading depend on how representative the specimen scale, loading path, and confinement are of real track conditions. Apparent contradictions between studies may thus reflect methodological differences as much as physical disagreement. (Indraratna, Ionescu & Christie, 1998; Indraratna, Sun & Nimbalkar, 2016; Rosa, Aragão & Motta, 2021.)

The fourth tension concerns the difference between ballast durability and whole-track performance. A grading that minimizes breakage in a triaxial cell is not automatically the grading that minimizes geometry deterioration in track, because track performance also depends on support stiffness, stiffness transitions, drainage evolution, and how often geometry correction is required. Berggren and Dahlberg both show that excessive stiffness, insufficient stiffness, and abrupt stiffness variation can all be harmful, albeit through different mechanisms. This means that the “best” ballast grading cannot be identified from particle breakage alone; it must also be judged against settlement, lateral resistance, track stiffness behavior, and maintenance robustness. (Berggren, 2009; Dahlberg, 2010.)

1.4 Modelling aspects

The Discrete Element Method (DEM) has become an increasingly important tool for studying the mechanical behavior of railway ballast, as it enables explicit representation of particle interactions, force transmission, and breakage mechanisms at the grain scale. A central challenge in DEM modeling of ballast is the representation of particle shape, which has been shown to strongly influence interlocking, dilatancy, and shear strength. While early studies relied on spherical particles for computational efficiency, more recent work has emphasized the need for non-spherical representations, such as clumps or polyhedral particles, to capture realistic behavior. However, increasing shape fidelity introduces additional model complexity and calibration demands, particularly in relation to contact detection, stiffness scaling, and computational cost.

Beyond particle shape, DEM modeling of ballast is critically dependent on the choice and calibration of contact models. Commonly used formulations, such as Hertz–Mindlin-type contact laws with frictional sliding, provide a reasonable first-order approximation, but their applicability to highly angular, rough, and potentially crushing aggregates remains an open question. Calibration is typically performed against laboratory tests, most often direct shear or triaxial compression, where relatively standardized datasets are available. In contrast, there is a notable lack of well-controlled experimental data for other loading scenarios, such as sleeper–ballast interaction tests, particularly in a Swedish context. This limits the ability to uniquely calibrate and validate DEM models for the specific boundary conditions and stress paths relevant to railway applications.

This gap motivates the need for combined experimental and numerical studies where DEM models are developed in parallel with carefully controlled physical tests. By establishing high-quality datasets for configurations such as the sleeper push test, it becomes possible to assess not only the influence of particle size distribution, but also the coupled effects of particle shape, morphology, and strength under realistic loading conditions. Such an approach enables a deeper, mechanistic understanding of ballast behavior, but it also places strict requirements on experimental repeatability, measurement resolution, and material characterization to ensure that the simulations can be meaningfully validated and used for predictive purposes.

1.5 Problem Formulation

Based on the current state of research, standards, and engineering practice, the following key research questions can be identified:

Is there a more optimal particle size distribution for railway ballast, and under what conditions?

- While current standards define acceptable grading envelopes, they do not prescribe a uniquely optimal solution. Ballast performance is governed by a complex interaction between particle size distribution, particle shape, lithology, packing state, and loading conditions. Furthermore, performance requirements are increasingly formulated in terms of functional criteria (e.g. deformation resistance, durability, drainage, and maintenance intervals), as emphasized in Trafikverket's approach to infrastructure design and material specification. This raises the question of whether alternative gradings, potentially tailored to specific material sources or functional applications (e.g. transition zones, high-speed lines, or maintenance-intensive sections), could provide improved long-term performance compared to current practice.

How can such an optimal or near-optimal particle size distribution be identified in a scientifically and practically robust manner?

- From both a research and engineering perspective, this represents a non-trivial challenge. Ballast behaviour emerges from coupled multi-scale mechanisms that are difficult to isolate experimentally and computationally. The design space is high-dimensional, involving grading shape, fines content, particle

morphology, and material strength, while also being constrained by aggregate production feasibility and standard requirements. Traditional empirical approaches and isolated laboratory tests are insufficient to systematically explore this space. This motivates a combined methodology where controlled experiments and advanced numerical simulations (DEM) are used in parallel to generate validated datasets and enable mechanistic interpretation. Such an approach provides a pathway to move from standard-based grading envelopes toward performance-informed and potentially optimized material design.

1.6 Objectives and Scope

The overall objective of this project is to perform an initial evaluation of how different scaled particle size distributions influence the mechanical behaviour and degradation of railway ballast.

Experimental objectives include:

- Designing and testing a limited set of representative PSDs
- Quantifying deformation, force response, and particle breakage
- Comparing behaviour across oedometer and sleeper push test configurations

Numerical objectives include:

- Establishing baseline DEM models corresponding to the experimental setups
- Demonstrating qualitative agreement between simulations and experiments
- Creating a foundation for future calibrated and predictive simulations

This study is explicitly positioned as a first evaluation, where a limited number of PSDs are investigated. A key outcome is not only the experimental observations themselves, but the development of validated DEM modelling frameworks. Once such models are established across multiple test types, they enable systematic exploration of a much wider design space of particle size and shape distributions in future work.

1.7 Limitations

Some limitations should be acknowledged when interpreting the results.

Scale effects:

The use of scaled particle size distributions for the oedometer tests implies that certain physical mechanisms, particularly those related to particle breakage and contact stress magnitudes, may not fully represent full-scale ballast behaviour.

It should be noted that this scaling is primarily driven by experimental constraints, specifically the specimen size imposed by the 170 mm diameter test cylinder. The scaling approach preserves the shape of the original PSDs and is consistently applied in both experiments and corresponding DEM simulations. As such, the scaling should be interpreted as a methodological requirement for experimental feasibility and consistency, rather than a numerical simplification.

For the sleeper push test, the DEM simulations are performed using particle size distributions that match the experimental materials as closely as possible, without

geometric scaling, enabling direct comparison between simulations and full-scale experimental conditions.

Simplifications in DEM:

In accordance with the original project scope and available resources, the numerical work has been restricted to the development of baseline DEM models and a limited set of simulations. A comprehensive parametric simulation campaign was therefore outside the scope of the present study.

The numerical models capture the dominant mechanical mechanisms governing ballast behaviour, but do not yet include all relevant physical processes. Most notably, particle breakage is not explicitly represented in the present simulations.

At the same time, it should be emphasized that the modelling framework operates at the current computational and methodological frontier of DEM for ballast applications. The use of dilated polyhedral particle representations enables a significantly improved description of particle interlocking, contact anisotropy, and force transmission compared to conventional spherical or clumped approaches. Furthermore, the simulations are executed at a scale close to practical limits, leveraging large-scale GPU-based computation to resolve particle systems of a size and complexity that remain inaccessible in most academic and industrial studies.

Despite this high level of fidelity, certain simplifications remain. Boundary conditions and geometrical representations are idealized, and the absence of particle fragmentation and contact models capturing local damage evolution limits the ability to reproduce long-term degradation and fines generation observed experimentally.

The current framework provides a direct pathway for further model enhancement. In particular, an advanced explicit fracture formulation based on Voronoi discretization of particles is available within the modelling environment and represents a key opportunity for future work. The integration of such models would enable simulation of crack initiation, propagation, and fragmentation processes, thereby significantly extending the predictive capability of the simulations.

Experimental constraints:

The experimental program was designed to prioritise the development and execution of test methodologies under realistic and practically feasible conditions. As a result, the number of tested particle size distributions and repetitions is limited.

From a practical perspective, the production of tailored ballast materials in intermediate tonnages is associated with significant cost, and transportation of such materials to the test facility represents an additional constraint. Furthermore, based on prior experience from the test facility in Karlskrona, the available test setup effectively limits the number of materials that can be handled and tested within a single campaign to approximately three.

While a broader range of particle size distributions and lithologies could in principle be evaluated, particularly within controlled laboratory testing such as oedometer experiments, such an extended test matrix was outside the scope of the present

study. This remains an important opportunity for future work, where a more systematic exploration of material variability can be conducted in a cost-efficient and targeted manner.

2 Methodology

2.1 Overall Approach

The project follows a combined experimental and numerical framework aimed at evaluating the influence of particle size distribution on the mechanical performance of railway ballast. The approach integrates controlled laboratory testing, large-scale physical testing, and Discrete Element Method (DEM) simulations to establish both empirical and mechanistic understanding of ballast behaviour.

The methodology is structured into four main stages:

- *Material definition* - Production and characterization of ballast materials with different particle size distributions, including standard, broadened, and bi-modal gradations.
- *Experimental testing* - Mechanical response is evaluated through large-scale sleeper push tests, cyclic oedometric testing, and complementary standard ballast tests.
- *DEM modelling* - Numerical models are constructed based on the experimental setups and calibrated using measured response data.
- *Comparison and evaluation* - Experimental and numerical results are compared to assess the influence of grading on stiffness, deformation, and degradation behaviour

3 Experimental Program

3.1 Materials

The materials used were produced by NCC Industry at the Hemmesjö quarry outside Växjö. The quarry was selected based on proximity to the Dynapac test facility in Karlskrona, enabling efficient transport and handling.

The following ballast types were produced and tested:

- M1: Standard class 1 railway ballast
- M2: Broader and less coarse ballast, produced through modified crushing and screening
- M3: Bi-modal distribution, consisting of M1 material blended with an additional coarse fraction
- M3.2: Controlled bi-modal distribution with 10 wt-% of 8–11.2 mm fraction added to M1

The bi-modal material (M3.2) was created by weighing the proportion of the two materials and mixing them on the asphalt area outside the test facility to ensure a controlled composition.

The materials (35 tons each) were transported to the test site by aggregate trucks and positioned in the test channel using a wheel loader and excavator. Special care was taken to minimize size segregation during handling.

After placement, the surface was levelled using an excavator and manually with rakes. The material was then compacted using a Dynapac CA3500 compactor with two static passes.

The channel geometry was documented using 3D laser scanning (FARO system) before filling, after filling, and after compaction, enabling detailed tracking of material distribution and settlement.

3.2 Particle Size Distributions

Sieve analyses were conducted at the NCC road laboratory in Hisingen, Kärra, to determine the particle size distributions of the investigated ballast materials (M1–M3), see Figure 1. Standardized sieving procedures were applied, and the cumulative passing (Q3) was obtained for each material across the relevant size range. The corresponding mass based frequency distributions (q3) are presented as histograms in Figure 2, providing a complementary view of the grading in terms of discrete size intervals. This representation facilitates comparison of the relative contribution of different size fractions between materials.

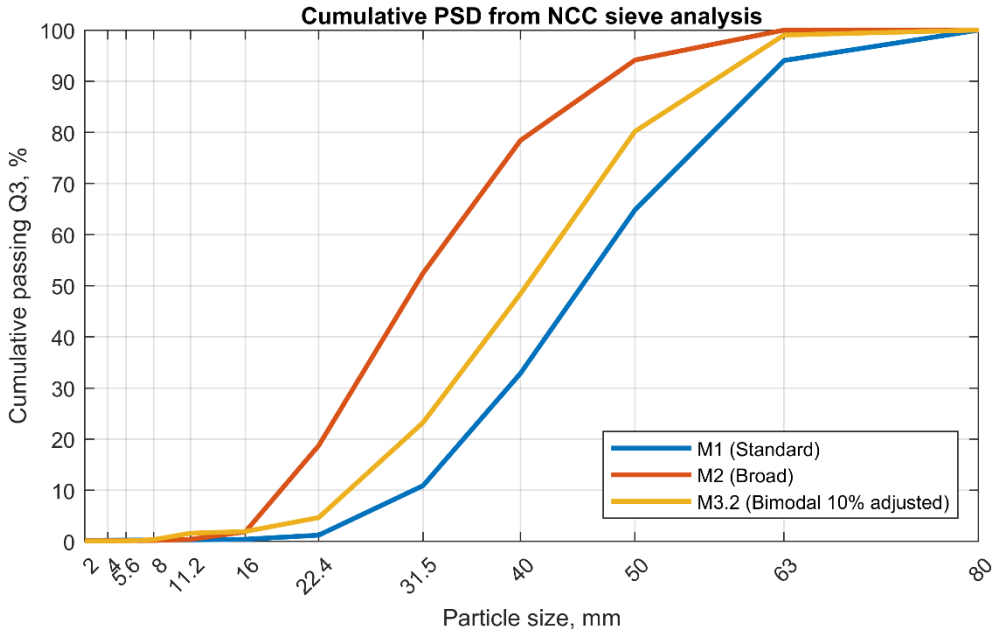

Figure 1. Particle size distribution of M1, M2, M3 based on the sampling performed on the beds after experiments.

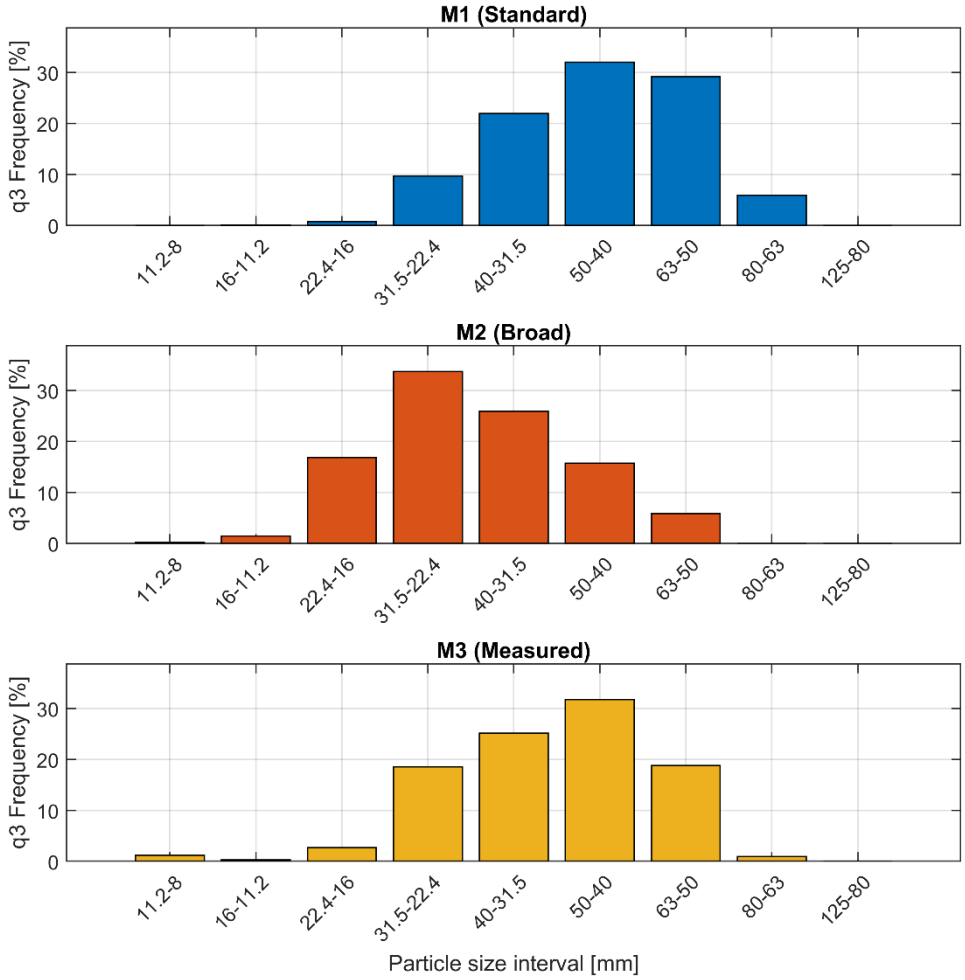

Figure 2. Particle size distributions expressed as mass-based frequency q3 for the original NCC ballast materials above 8 mm. M1 (standard grading) exhibits a coarse-dominated distribution with a peak in the 40–63 mm range, M2 (broad grading) shows a wider spread with increased content in intermediate sizes, and M3 (measured) displays a slightly more balanced distribution with reduced coarse fraction and increased mid-size material. Note that the measured M3 distribution does not reflect the intended bi modal mix with 10% of the 8 to 11.2 mm fraction.

For the oedometer tests, it is not possible to perform the experiment with real top size at 63-80mm. Therefore a scaling approach was applied to scale the size distribution to a top size of 22.3mm. The original particle size distribution (PSD) was geometrically scaled to match the target size range of the laboratory tests. This was achieved by applying a constant scaling factor to the particle diameters, while preserving the cumulative passing distribution (Q3). Only the physically relevant size range was scaled, excluding oversized particles outside the target domain.

Following scaling, the PSD was interpolated onto a predefined set of target sieve sizes using linear interpolation in logarithmic particle size space. This approach ensures a smooth and physically consistent redistribution of mass between size classes, while maintaining the overall shape of the original distribution. An illustration of this procedure is shown in Figure 3, while the resulting scaled and interpolated particle size distributions for all investigated materials are presented in Figure 4.

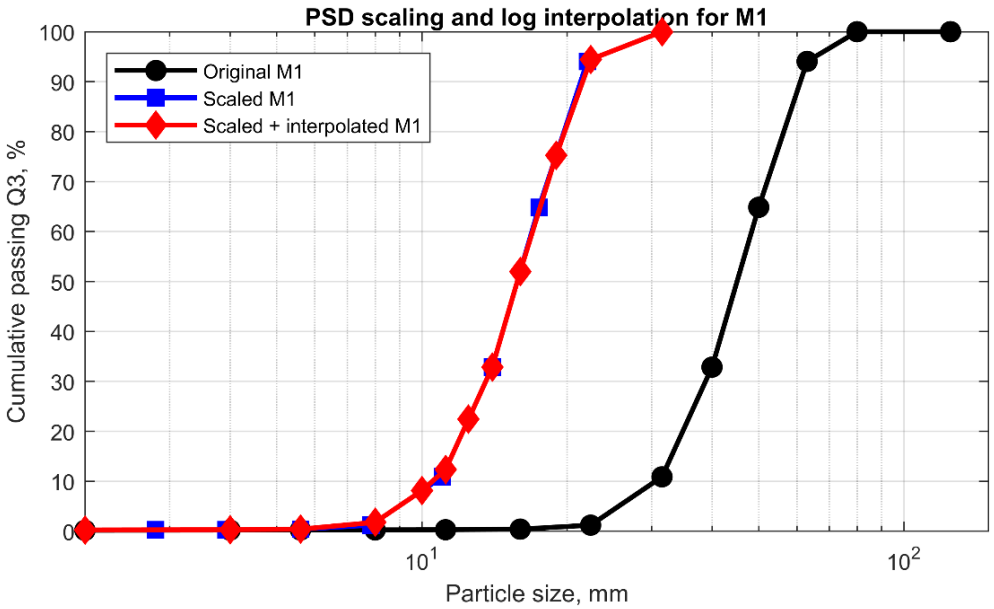

Figure 3. Illustration of the scaling and interpolation procedure in order to facilitate scaled samples for the oedometer tests.

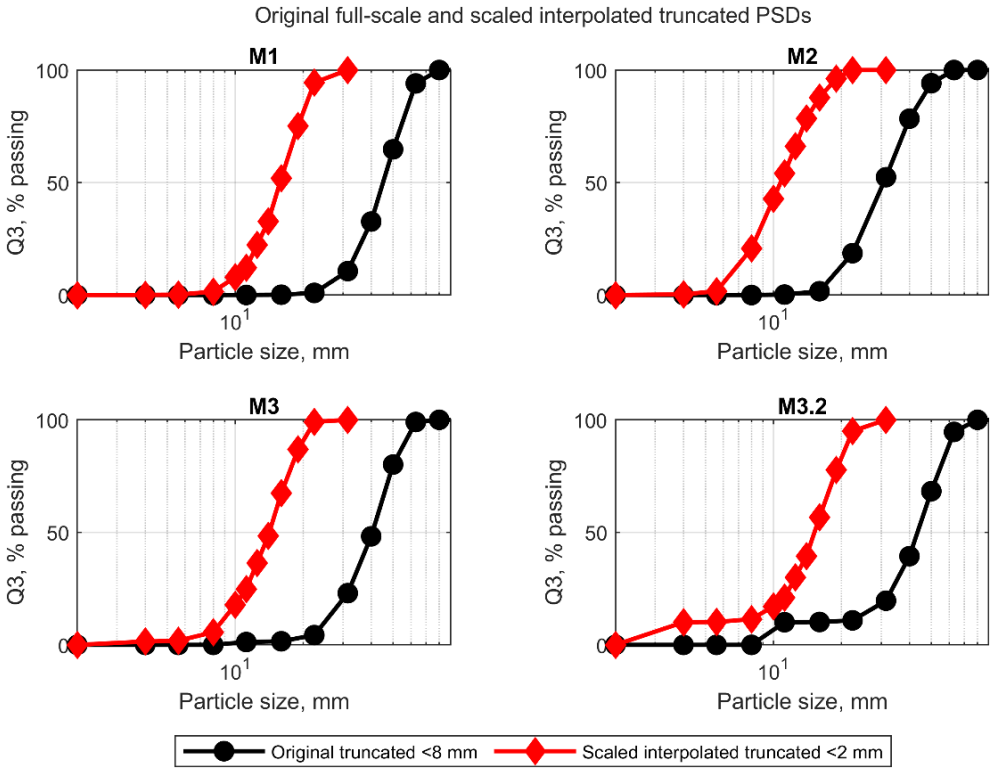

Figure 4. Original and scaled particle size distributions (PSDs) for all investigated materials (M1, M2, M3, M3.2). The original truncated distributions (black) are compared with the geometrically scaled and interpolated distributions (red), adapted to the reduced size range required for the oedometer tests. The scaling preserves the overall shape of the PSDs while truncating the upper size range and redistributing mass consistently across particle sizes.

3.3 Sleeper Push Test

3.3.1 Development of the Test Method

The sleeper push test was developed to evaluate alternative railway ballast size distributions under controlled but representative conditions. The intention was to capture the mechanical response of ballast subjected to lateral loading, while maintaining a test configuration that allows for controlled boundary conditions and repeatability.

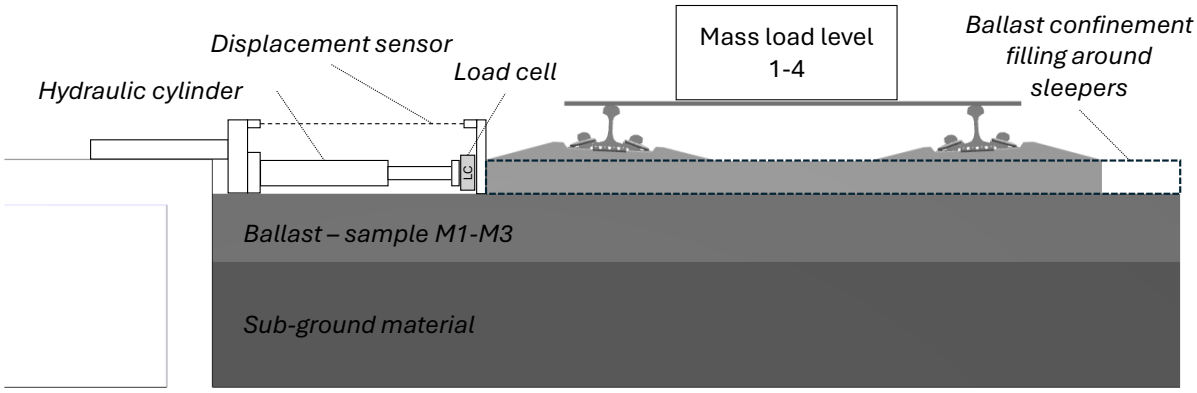

Figure 5. Schematic illustration of the sleeper push test setup, showing the hydraulic loading system acting on the central sleeper, the ballast layer (materials M1–M3), underlying subgrade, and applied vertical mass loading levels.

In the literature, sleeper push tests are commonly performed using a simple hydraulic jack with a manual pump. While this solution is low cost and straightforward, it is not preferable in this context, as each loading sequence re-activates friction, leading to reduced control and repeatability. To address this, a hydraulic system was instead rented from Walleverken.

The test setup was designed around three A32 sleepers with a centre-to-centre spacing of 600 mm. The use of three sleepers was motivated by the need for a stable construction and the ability to apply load to the middle sleeper. A single-sleeper configuration would make it practically difficult to apply a vertical load, while a two-sleeper configuration would require a more complex loading arrangement acting between the sleepers.

Figure 6. Left: Picture of A32 sleepers. Right: Section with mounted 60E1 rail and fasteners.

The loading system was designed and arranged by the engineering team at Dynapac. A welded sheet metal device was constructed to transfer load from the hydraulic cylinder to the concrete slab edge of the test channel. The device also allowed for height adjustment, ensuring that the hydraulic cylinder remained horizontal and aligned with the load cell mounted on the middle sleeper. A cylindrical plate load cell was installed on the middle sleeper, including a connection joint to the hydraulic cylinder piston.

Figure 7. Left: The developed assembly to hold and align the hydraulic cylinder. Right: complete system setup with hydraulic system and sensors.

One key challenge during pre-testing was achieving a loading direction that was truly parallel. This was resolved by introducing two equal-length wooden beams placed between the concrete slab and the outer sleepers. A laser line was then aligned orthogonally through the centre of the hydraulic cylinder, load cell, and sleeper system, extending to a reference point on the opposite concrete wall. Minor angular deviations were recorded for each test, and the distances between the outer sleepers and the concrete edge were measured after each test.

Figure 8. Left: channel filled with material M1-M3 before static compaction. Right: During static roller compaction.

Figure 9. Left: Example picture of the unconfined C1 condition. Right: example picture of the confined C2 condition.

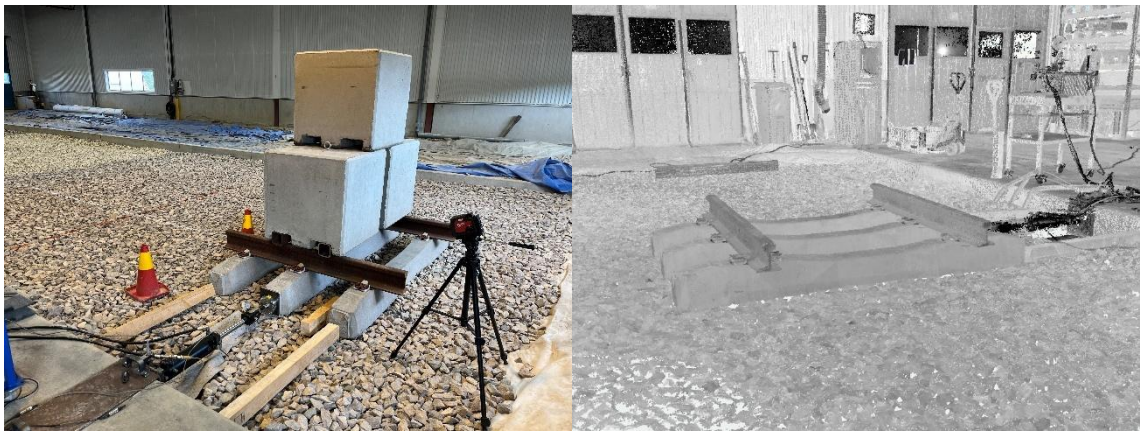

Figure 10. Left: Test setup in the R4 loading condition with three concrete blocks. Right: Example image from the laser 3D scanning point cloud.

3.3.2 Test Procedure

The material was transported to the test site and placed in the channel using a wheel loader and excavator. Special care was taken to minimize size segregation during handling. The M3 material was prepared by weighing the proportions of the two components and mixing them on an asphalt surface outside the test facility.

After placement, the surface was levelled using an excavator and manually with rakes, followed by compaction using a Dynapac CA3500 compactor with two static passes.

The test channel was 3D scanned using a FARO laser scanner at six positions before material placement, after filling, and after compaction.

Four Geokon 3515 ground pressure sensors were installed beneath the ballast. The sensor layout was designed to capture stresses beneath the rail-sleeper fastening locations, particularly under the middle sleeper. Due to a limited number of sensors, positions further away under the outer sleepers were selected.

Each test was conducted according to the following procedure:

- Positioning or re-positioning of the rig, ensuring parallelism and alignment using the centre laser line
- For the confined (C2) condition, repositioning of ballast on the shoulder and sides
- Placement of concrete blocks to apply vertical load (tests R2–R4)
- Connection of the hydraulic cylinder piston
- Connection of displacement sensors
- 3D laser scanning of the initial state
- Start of data acquisition and camera recording
- Application of a trigger load signal on the sleeper for synchronization of data and video
- Initiation of loading using the hydraulic system
- Termination of the test at approximately 50 mm displacement
- Stopping data acquisition and camera recording
- Final 3D laser scanning
- Disconnection of piston and sensors
- Measurement of outer sleeper positions

The vertical loading in the sleeper push tests was applied by combining the self-weight of the sleeper–rail assembly with additional discrete concrete masses placed on top of the rails. This approach enables a controlled variation of the normal load acting on the ballast, thereby allowing the influence of confinement on shear resistance and deformation behaviour to be systematically evaluated.

The loading was increased incrementally across four predefined load cases (R01–R04), where each step corresponds to the addition of one concrete block with a mass of approximately 1.1 tonnes, see Table 1. The baseline case (R01) represents the inherent load from the sleepers and rails only, while the subsequent cases introduce progressively higher vertical stresses.

Table 1. Applied vertical load configurations for the sleeper push tests. The total mass and corresponding vertical force are shown for each load case (R01–R04), where the loading is increased incrementally by adding concrete blocks (1.1 ton each) on top of the sleeper–rail assembly. The baseline case (R01) represents the self-weight of sleepers and rails only.

Load case	Number of concrete blocks	Total mass [kg]	Total force [N]	Description
R01	0	1072.2	10 526	Sleeper + rails only (baseline)
R02	1	2172.2	21 309	Sleeper + rails + 1 concrete block
R03	2	3272.2	32 092	Sleeper + rails + 2 concrete blocks
R04	3	4372.2	42 875	Sleeper + rails + 3 concrete blocks

3.4 Oedometer Tests

The oedometer tests were performed using an Instron 400RD testing rig. The ballast material was placed in a rigid cylindrical container shown in Figure 11 which dimensions are summarized in Table 2. The specimen was confined laterally by the cylinder walls, while vertical loading was applied through a rigid loading plate. The setup ensures one-dimensional compression conditions, where radial deformation is restrained and particle rearrangement occurs primarily in the vertical direction.

A monotonic vertical load was applied at a constant loading rate of 125 kPa/s up to a maximum stress of 500 kPa. The loading was continuous without unloading phases, ensuring a consistent stress path across all tested materials. The selected loading rate represents a compromise between test duration and minimizing rate-dependent effects.

The applied vertical load and corresponding displacement were continuously recorded throughout the test. From these measurements, stress–strain relationships were derived, allowing evaluation of compressibility and stiffness characteristics of the ballast materials. The data also enable comparison of deformation behaviour between different particle size distributions.

Figure 11. Photo of the test cylinder with sample prepared (right) and during loading in the Instron 400RD (right).

Table 2: Dimensions of oedometer rig.

Dimensions	Parameter	Value	Unit
Height of cylindrical shell (reducing the length from the plug)	h	0.095	m
Diameter of cylindrical shell/piston	d	0.17	m
Piston bottom area	a	0.0227	m^2
Volume inside oedometer shell	V	2.15×10^3	m^3
Weight of piston	m	22	kg
Self weight of piston	F_{mg}	215	N

To obtain a representative measure of stiffness, the stress–strain response was evaluated in the near-peak loading regime. Specifically, the loading branch of each cycle was identified, and a linear regression was applied to the stress–strain data within 60–95% of the peak stress. This approach provides a consistent and robust estimate of the oedometric stiffness, while avoiding initial non-linearities associated with particle rearrangement and seating effects. An example of this procedure is illustrated in Figure 12.

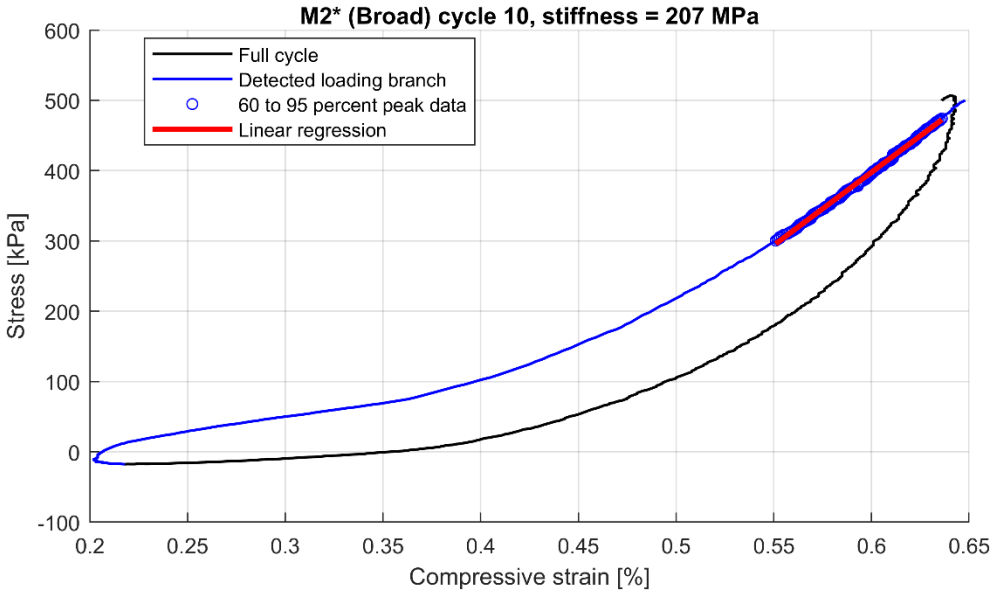

Figure 12. Stress–strain response for material M2 (broad grading) during cycle 10 of the cyclic oedometer experiment. The full hysteresis loop is shown (black), with the detected loading branch highlighted (blue). Stiffness is evaluated from the near-peak region (60–95% of peak stress), where a linear regression (red) is applied to determine the representative oedometric stiffness (207 MPa).*

3.5 Standard Ballast Tests

In addition to the experimental test methods described above, the materials were characterized using standard test methods for railway ballast in accordance with relevant European standards. These tests include particle size distribution (SS-EN 933-1), resistance to wear (Micro-Deval, SS-EN 1097-1/A1), resistance to fragmentation (Los Angeles, SS-EN 1097-2/A1), particle shape (flakiness index, SS-EN 933-4), and assessment of oversized grains in accordance with SS-EN 13450.

The results from these standardized tests are summarized in Table 3. Overall, the materials show comparable mechanical quality in terms of wear and fragmentation

resistance, while differences are primarily observed in particle size distribution and shape characteristics, reflecting the intended variations between M1, M2, and M3.

Table 3. Summary of material properties and standard test results for ballast materials M1, M2, and M3, including particle size distribution, Micro-Deval (MDE) resistance, Los Angeles (LA) abrasion, proportion of oversized particles, and flakiness index (SI) in accordance with relevant SS-EN standards.

Test type	Unit	M1	M2	M3
SS-EN 933-1 Size distribution				
SS-EN 1097-1/A1 Micro Deval (MDE) RB		5	6	5
Analysis sample A	%	5.2	5.7	4.9
Analysis sample B				5.2
SS-EN 1097-2/A1 Los Angeles (LA) RB		15	16	15
SS-EN 13450 grains with length > 100mm [EA]				
Value	%	16	4	8
Fraction	mm	31.5-80	31.5-80	31.5-80
SS-EN 933-4 LT-index (SI)	-	16	-	18

4 Numerical Modeling (DEM)

4.1 Modeling Strategy

The Discrete Element Method (DEM) was used to complement the experimental program by providing insight into particle-scale mechanisms governing the macroscopic response observed in the tests. In particular, the simulations were used to analyze force transmission, particle rearrangement, and the influence of particle size distribution on bulk behaviour in both the oedometer and sleeper push configurations. All simulations were performed using the Demify software.

The oedometer simulations were executed on NVIDIA RTX 5080 GPUs, while the more computationally demanding sleeper push simulations were performed on NVIDIA H200 hardware.

4.2 Particle Representation

Particles were represented using the dilated polyhedral model available in Demify. This representation allows for more realistic interlocking and contact behaviour compared to spherical particles, while maintaining computational efficiency relative to fully resolved polyhedral geometries.

To model the ballast particles, ten different rocks with simplified scans consisting of 20 and 24 triangles serve as a basis for the simulation. The particle size distributions were scaled to match the reduced laboratory geometries, following the methodology described above. Oversized particles outside the target size range were excluded, and the resulting distributions were interpolated in logarithmic space to ensure a smooth and consistent representation.

All simulations employed the Hertz–Mindlin–Deresiewicz (HMD) contact model to describe normal and tangential interactions between particles. This model accounts for non-linear elastic contact behaviour and history-dependent tangential forces, providing a realistic representation of granular contact mechanics.

4.3 Sleeper Push Test Model

4.3.1 Geometry and Boundary Conditions

A mesh of the subground is generated from the 3D-scans taken before the experiments. The locations of all the Geokon sensors are also retrieved from this 3D-scan. A CAD model of the sleeper push rig is created with three concrete blocks, which are used in the following DEM-simulations. In order to reduce the number of DEM-particles in the simulation, and in turn decrease the computational cost, a smaller domain is created in which the particle bed is located, with walls on each side that contain the particles. A visual representation of the simulation setup is shown in Figure 13. All rigid objects (ground mesh, sleeper push rig, Geokon sensors) are set to the same concrete material, which helps reduce the number of calibration parameters.

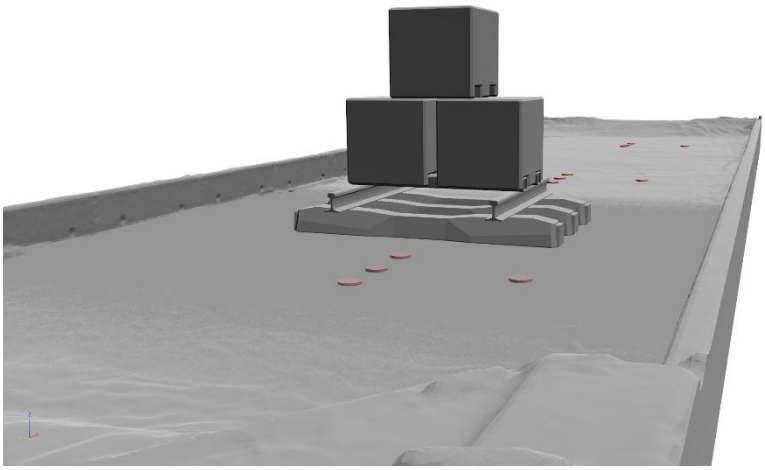

Figure 13. Image from the DEM model setup of the sleeper push test rig in the R4 condition.

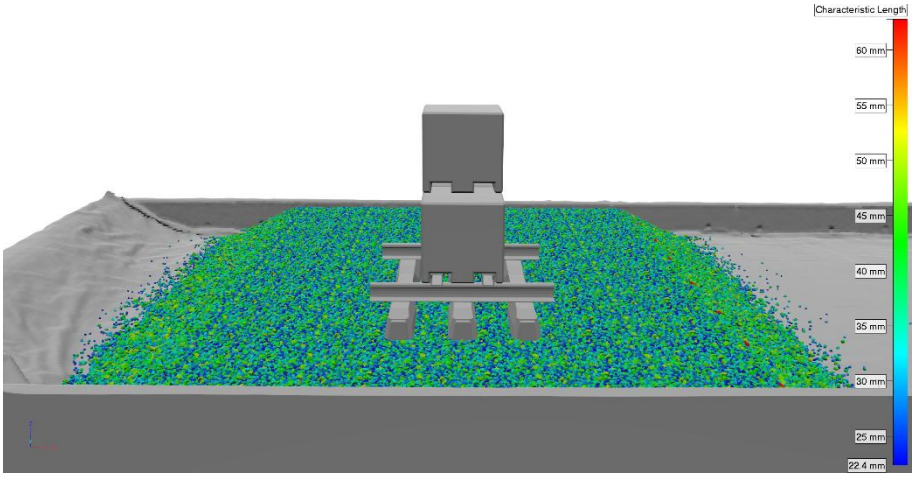

Figure 14. Image from the DEM initial condition, front view.

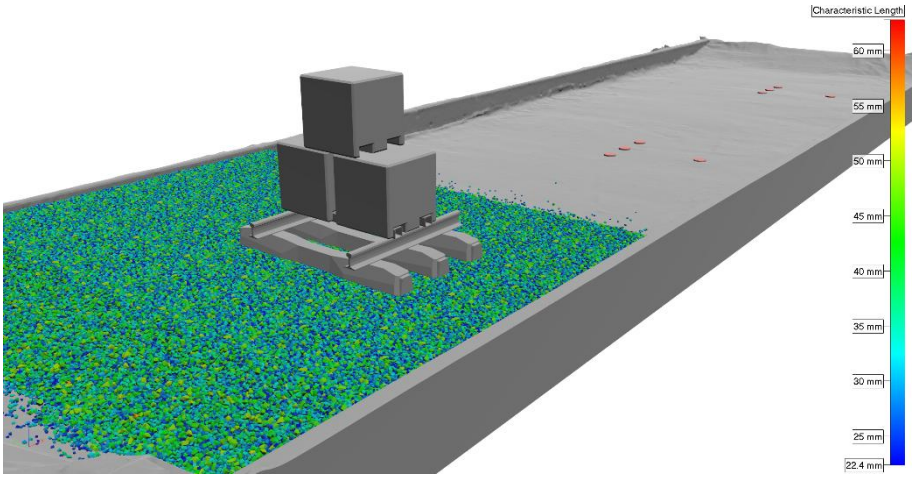

Figure 15. Image from the DEM initial condition, iso view.

4.3.2 Loading Implementation

The sleeper push rig is treated as a rigid object in the DEM model, where the velocity is set and updated according to a chosen interval. For all simulations in this report, this communication time step interval is set to 1e-3. Translation in X, along with rotation around Y and Z are locked, which means that the remaining degrees of freedoms are controlled by updating the velocity in each communication step. For translation in Y, a constant velocity is set, which models the motion induced by the hydraulic cylinder. Translation in Z, along with rotation around X, is controlled by integrating their respective motions. The following equation is integrated using the forward Euler method to get the velocity. F_g is here the weight of the rig, F_{DEM} is the reaction force in Z from the particles on the sleepers, which is calculated from the DEM model, m is the mass of the rig and a_z is the acceleration in Z of the rig.

$$F_g + F_{DEM} = m * a_z$$

For the rotation around X, the following equation is integrated using Forward Euler to get the rotational velocity. M_{DEM} is the moment around X calculated from the DEM model, I_{rig} is the moment of inertia around X calculated from the CAD model and α_x is the rotational acceleration around X.

$$M_{DEM} = I_{rig} * \alpha_x$$

The constant velocity of the translation in Y is estimated from the experimental data to be 4.23 m/s.

4.3.3 Output Quantities

The asymptotic force is retrieved from the force-displacement, and it is calculated as the mean force between 30mm and 40mm of displacement. The difference in the rig position in Z between the start and the end of the simulation is also studied as a measure of settlement.

4.4 Oedometer Model

4.4.1 Geometry and Boundary Conditions

The model setup of the oedometer simulation is shown in Figure 16 and consists of a cylindrical shell, a bottom plug, and a piston. These components are obtained from a CAD model with the same dimensions as the physical test equipment and are summarized in Table 2. All components are made of steel and the entire oedometer rig is treated as a rigid object in the DEM-model. The shell and bottom plug are fixed, while the piston moves vertically to apply a known pressure to the particle bed. This movement is regulated as described in more detail in Section 4.4.2.

Figure 16: The oedometer rig consists of a cylindrical shell (purple), plug at the bottom (yellow) and a piston (blue). The oedometer is filled with a particle bed (grey).

The ballast particles are modelled with the particle representation described in Section 4.2. In total, the oedometer is filled with 2750 g of particles to get a bed height around 80-85mm. The same scaled size distribution as in the experiments is used in the simulations, see Figure 30. However, particles below 5.6 mm are excluded in the simulation to allow for larger timesteps in the DEM simulation which is set to 5×10^{-7}s. Therefore, M3.2 is excluded in the simulations since a larger part of this material consists of small fines, whereas particles below 5.6 mm only make up around 1% of the particle distribution for M1 and M2.

The oedometer rig is made from steel while the ballast particles consist of granite. The material parameters as well as the interactions are defined in Table 4. Interaction forces are calculated using the Hertz-Mindlin-Deresiewicz (HMD) contact model.

Table 4: Material parameters and interactions.

Parameter	Variable	Value	Unit
Granite density	ρ	2700	kg/m^3
Granite Young's modulus	E	40	GPa
Granite Poisson's ratio	ν	0.2965	-
Steel density	ρ	7800	kg/m^3
Steel Young's modulus	E	20	GPa

Steel Poisson's ratio	ν	0.3	-
Granite-granite friction	μ	0.700	-
Granite-granite restitution		0.633	
Steel-granite friction	μ	0.400	-
Steel-granite restitution		0.424	-

4.4.2 Loading Implementation

To apply a prescribed pressure from the piston to the particle bed, a Proportional–Integral (PI) controller is implemented using a cyclic trapezoidal pressure as reference. The reference pressure follows the same pressure rate and maximum pressure used in the experiments. Although pressure is the target variable, the controller operates by adjusting the piston velocity $v(t)$ at time t during the DEM simulation, with updates every 1×10^{-3} s.

Before the piston comes in contact with the particle bed ($p_{\mathrm{sim}}(t) \leq p_{\mathrm{contact}}$), the simulation is initialized with a linearly varying velocity. After this initialization phase, the load is regulated using the PI controller. The velocity is thus defined as

$$v(t) = \begin{cases} v_{\mathrm{init}} - 1.1t, & p_{\mathrm{sim}}(t) \leq p_{\mathrm{contact}} \\ \min\left(K_{\mathrm{p}} e(t) + K_{\mathrm{i}} \int_0^t e(\tau) d\tau \, , v_{\mathrm{max}}\right), & p_{\mathrm{sim}}(t) \leq p_{\mathrm{contact}} \end{cases}$$

where

$$e(t) = p_{\mathrm{sim}}(t) - p_{\mathrm{ref}}(t)$$

is the control error comparing the simulated vertical pressure p_{sim} and the reference vertical pressure p_{ref}. The parameters K_{p} and K_{i} represent the proportional and integral coefficients, respectively, and are tuned for this application. The controller's output is limited by v_{max} to prevent excessive oscillations. The selected parameters are summarized in Table 5 and the regulation of the cyclic trapezoidal pressure is shown in Figure 17. From the figure, the regulator quickly reaches the desired response.

Table 5: Load setup used in simulation.

Parameter	**Variable**	**Value**	**Unit**
Initial velocity	v_{init}	0.3	m/s
Max regulated velocity	v_{max}	0.1	m/s
Preload pressure	p_{contact}	18	kPa
Load rate		125	kPa/s
Maximum load	p_{max}	500	kPa
Proportional coefficient	K_{p}	3e-8	-
Integral coefficient	K_{i}	1e-10	-

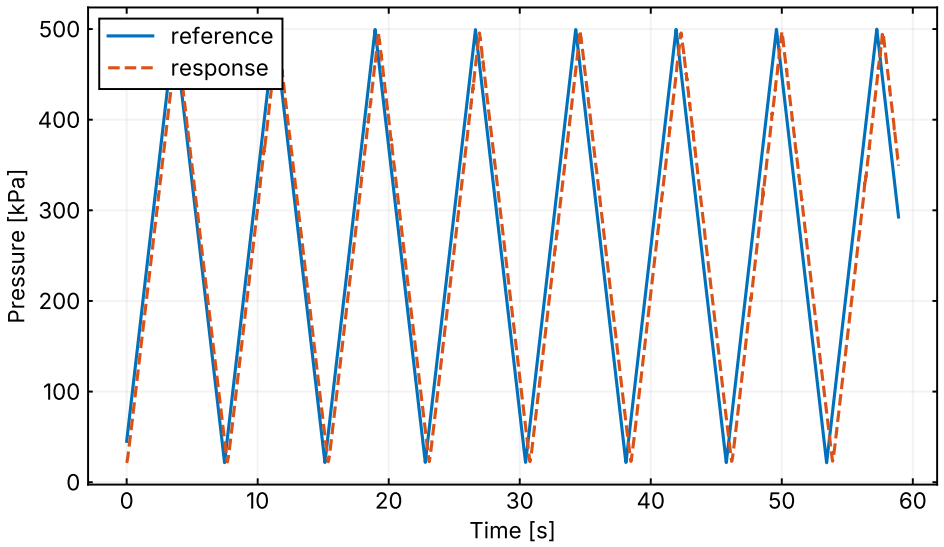

Figure 17: Pressure regulation using a PI controller. The simulated pressure (response) tracks the reference signal.

4.4.3 Output Quantities

From the simulation data, the pressure (and corresponding force), together with the deformation of the particle bed, can be extracted, enabling an estimation of strain. Based on these quantities, the stiffness of the particle bed is determined for each loading cycle using the minimum and maximum stress–strain values, allowing its evolution over time to be assessed.

In the post-processing stage, the initial cycle is excluded, as the particle bed initially needs to be flattened, which results in large displacements that are not representative of the subsequent response.

5 Experimental Results

5.1 Sleeper Push Test Results

5.1.1 Force-displacement behavior

The force–displacement responses for all materials and loading conditions are presented in Figure 18 to Figure 23. The results exhibit a consistent overall behaviour characterized by an initial rapid increase in resistance at small displacements, followed by a gradual transition towards an asymptotic force level. This behaviour reflects the progressive mobilization of particle interlocking and force chain development within the ballast layer.

A clear and dominant trend across all materials is the strong influence of vertical loading (R01–R04) and confinement condition (C1 vs C2). Increasing vertical load leads to a systematic increase in mobilized resistance, with higher load cases exhibiting both

steeper initial stiffness and higher asymptotic force levels. Similarly, the confined condition (C2) consistently results in significantly higher resistance compared to the unconfined condition (C1), indicating that lateral confinement plays a critical role in stabilizing the granular structure and enhancing shear transfer. For material M1 (Figure 18–Figure 19), the response under C1 shows relatively limited resistance for lower load cases (R01–R02), with a clear separation emerging as vertical load increases. Under C2, the response is markedly amplified, with higher load cases reaching substantially greater force levels and exhibiting a more stable plateau behaviour. The variability between repetitions is relatively low at higher loads, indicating a more stable force chain structure under increased confinement.

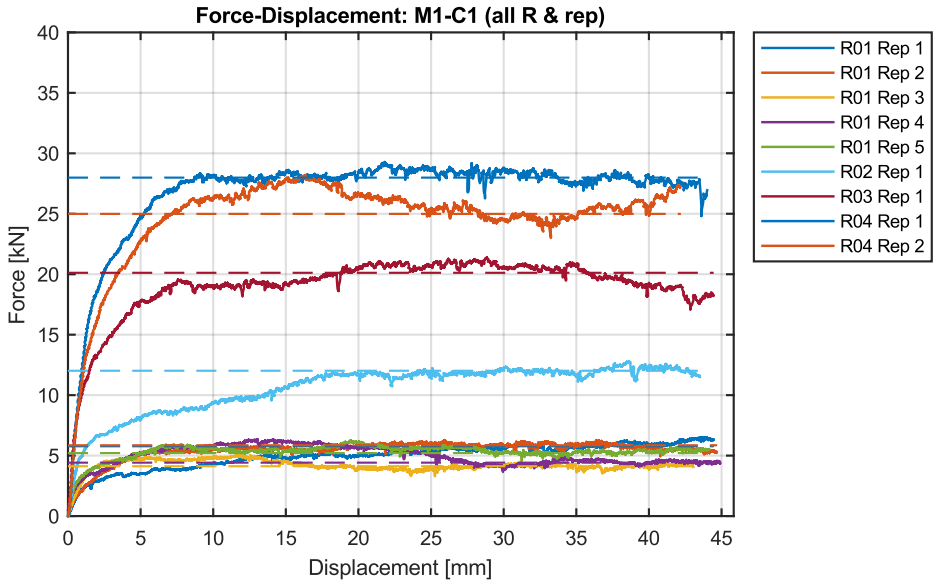

Figure 18. Force–displacement response for material M1 (Standard) under condition C1 (Unconfined) in the sleeper push test.

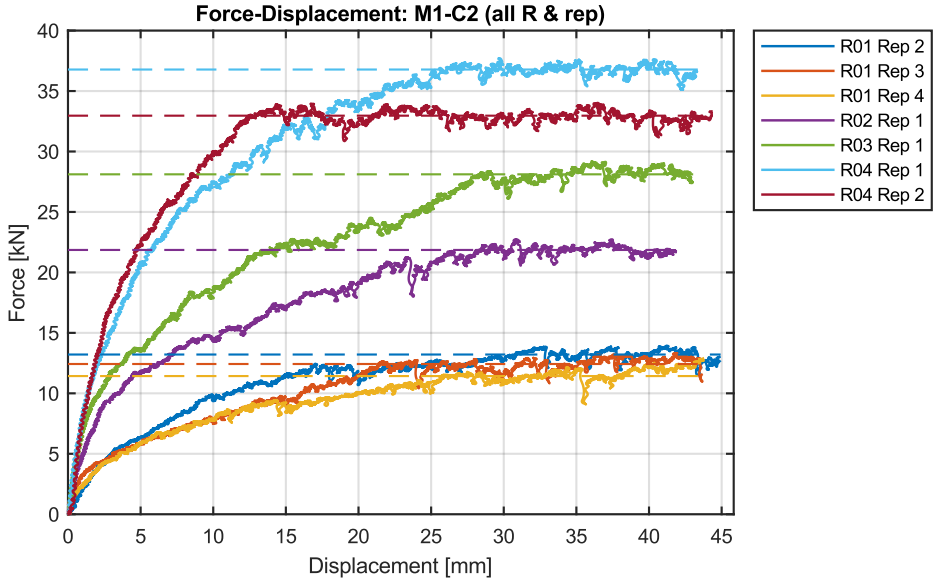

Figure 19. Force–displacement response for material M1 (Standard) under condition C2 (confined) in the sleeper push test.

For material M2 (Figure 20–Figure 21), a similar overall trend is observed, but with a slightly more gradual force development and, in some cases, increased variability at larger displacements. Under C1, the highest load cases (R03–R04) reach force levels comparable to M1, but the transition to the asymptotic regime appears less sharp. Under C2, M2 exhibits a strong increase in resistance, although with some indications of instability or sudden drops in force for individual repetitions, suggesting local rearrangements or failure events within the particle structure.

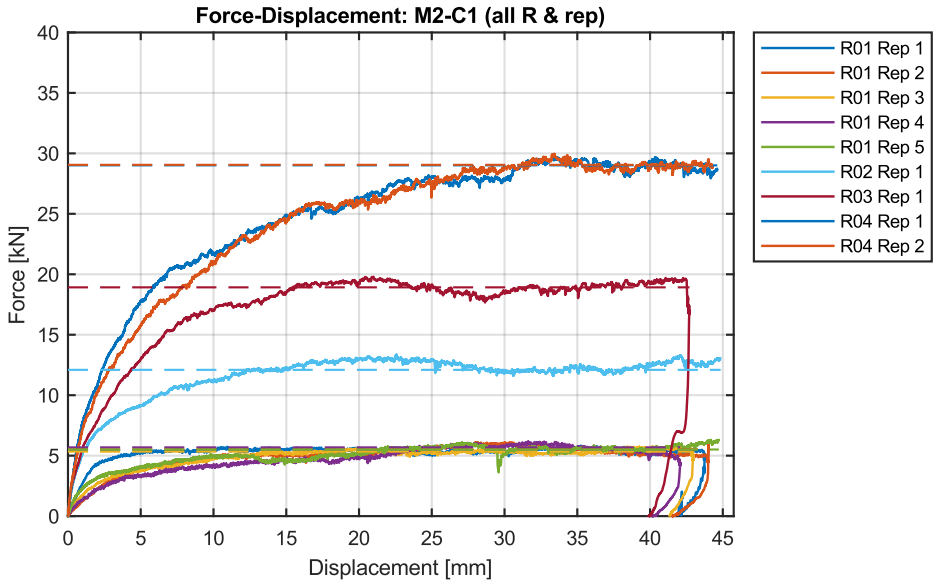

Figure 20. Force–displacement response for material M2 (Broad) under condition C1 (Unconfined) in the sleeper push test.

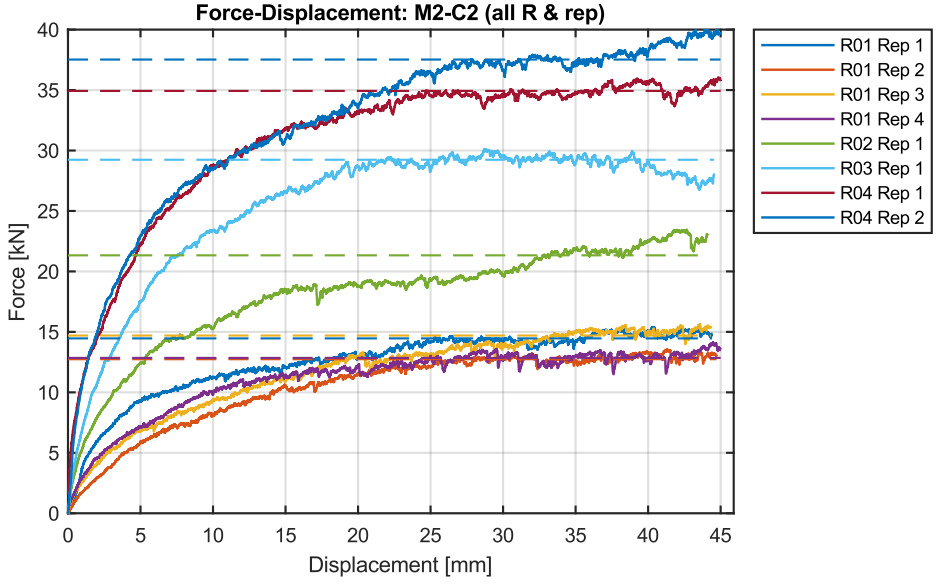

Figure 21. Force–displacement response for material M2 (Broad) under condition C2 (Confined) in the sleeper push test.

For material M3 (Figure 22–Figure 23), the response is generally smoother, with a more gradual mobilization of resistance across all load levels. Under C1, the asymptotic

force levels are comparable to M1 and M2 for higher loads, but the initial stiffness is slightly lower. Under C2, M3 demonstrates a pronounced increase in resistance, similar in magnitude to the other materials, but with a more continuous and less abrupt transition to peak behaviour, indicating a more distributed load transfer mechanism.

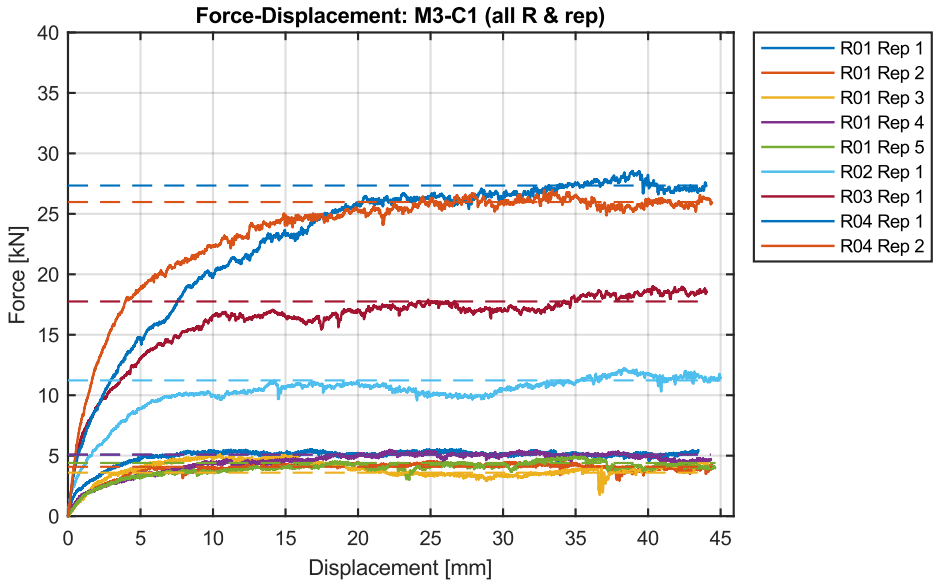

Figure 22. Force–displacement response for material M3 (Bi-modal) under condition C1 (Unconfined) in the sleeper push test.

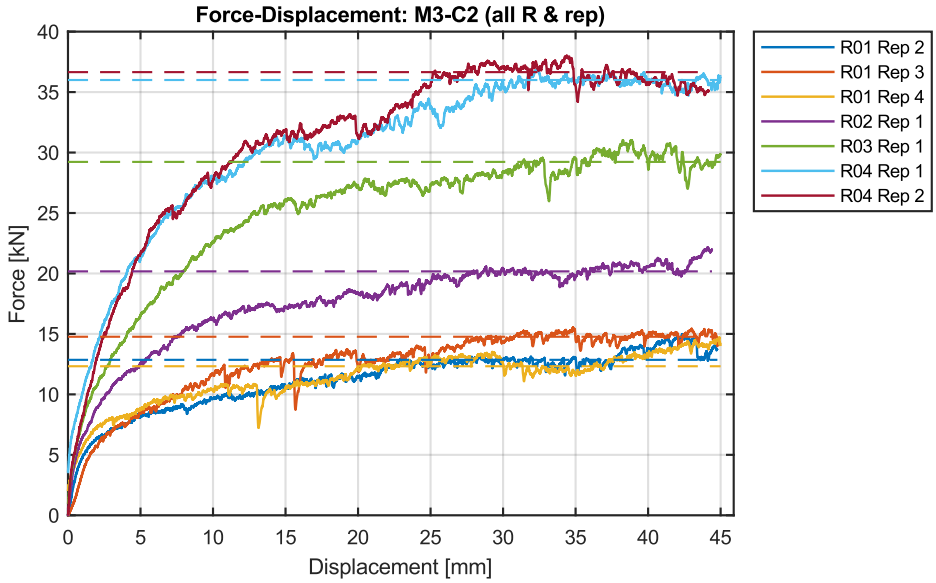

Figure 23. Force–displacement response for material M3 (Bi-modal) under condition C2 (confined) in the sleeper push test.

The dashed horizontal lines in the figures, representing the asymptotic force levels, indicate that despite local fluctuations, the responses converge towards consistent mean resistance values for each load case.

To summarize, the force–displacement results demonstrate that:

- Vertical load and confinement are the primary drivers of lateral resistance in the sleeper push test
- All materials exhibit similar qualitative behaviour, with differences mainly in stiffness development and smoothness of response
- The asymptotic resistance is well-defined and increases systematically with load level
- Variability between repetitions remains limited and consistent across load levels, supporting the robustness of the experimental setup

These observations provide the basis for the subsequent characterization of shear strength using Mohr–Coulomb type analysis.

5.1.2 Shear Strength Characterization

The derived Mohr–Coulomb envelopes, see Figure 24, show a consistent and near-linear relationship between shear stress and normal stress for all tested materials and confinement conditions. The friction angle (φ) remains within a relatively narrow range (approximately 30.5°–32.5°), indicating that the frictional component of shear strength is largely insensitive to the particle size distribution.

In contrast, the apparent cohesion (c) shows a clear dependence on the confinement condition. For all materials, the C2 condition results in a significant increase in cohesion compared to C1, reflecting the influence of lateral confinement and particle interlocking. This suggests that boundary conditions and packing state have a stronger impact on shear strength than the grading itself.

Comparing the materials, only minor differences are observed. M2 exhibits a slightly higher friction angle, while M1 and M3 shows comparable behaviours. The cohesion values under confined conditions (C2) are similar across all materials, indicating that the effect of increased confinement dominates over differences in particle size distribution.

The results suggest that while particle size distribution influences other aspects of ballast behaviour, its direct effect on Mohr–Coulomb shear strength parameters is secondary compared to confinement effects.

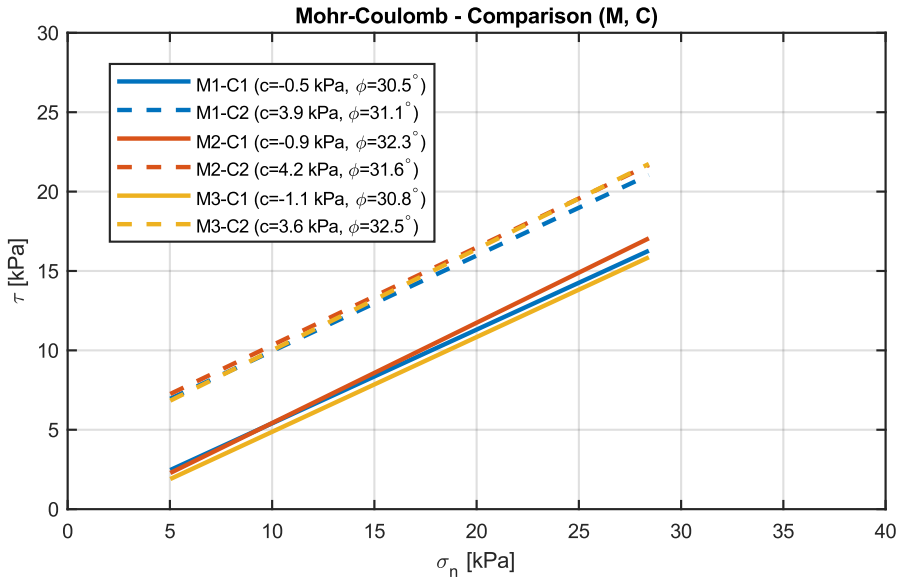

Figure 24. Mohr–Coulomb failure envelopes for materials M1 (standard), M2 (broad), M3 (bi-modal) under confinement conditions C1 (unconfined) and C2 (confined), derived from the sleeper push tests. The fitted cohesion (c) and friction angle (φ) are indicated in the legend for each case. The results show a consistent increase in apparent cohesion under the more confined condition (C2), while the friction angle remains relatively similar across materials and test conditions.

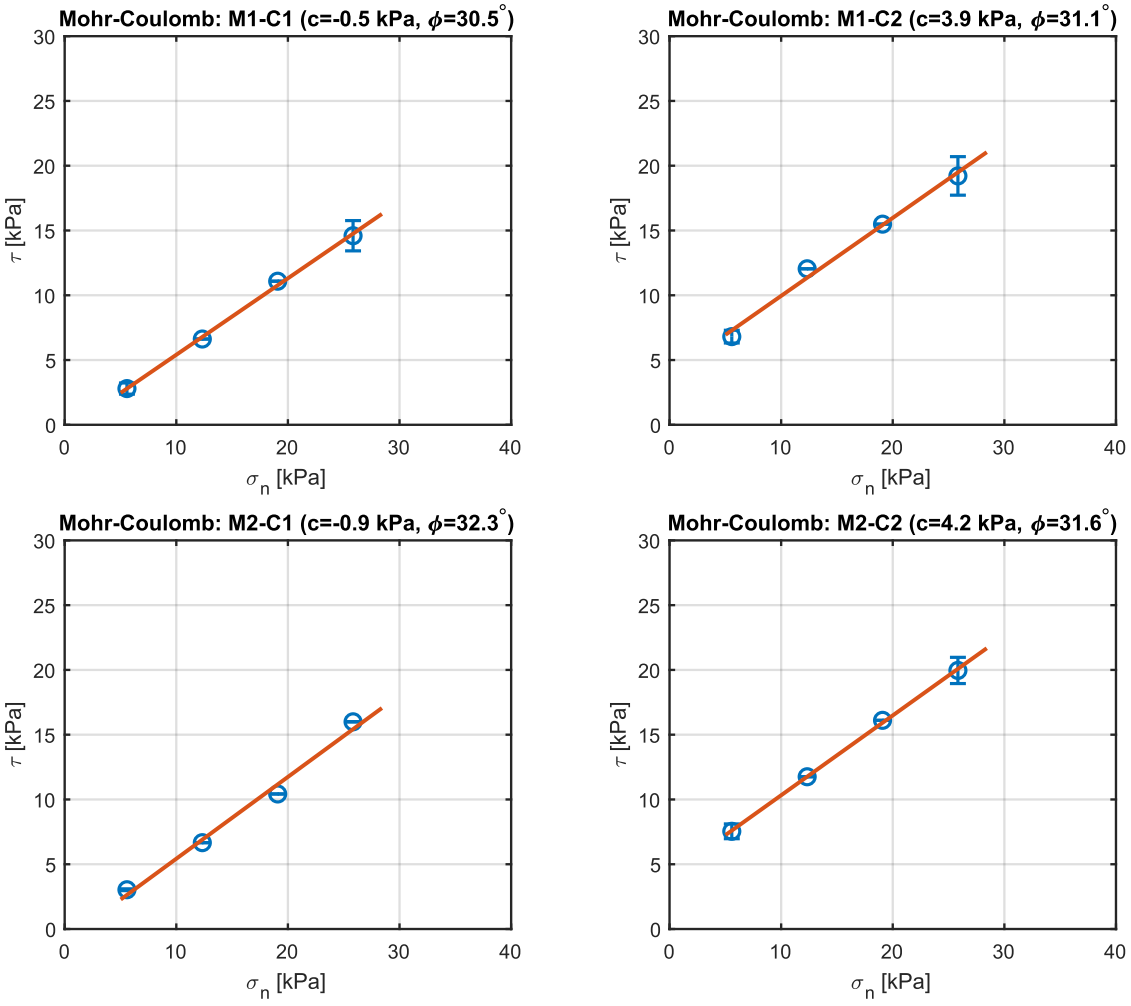

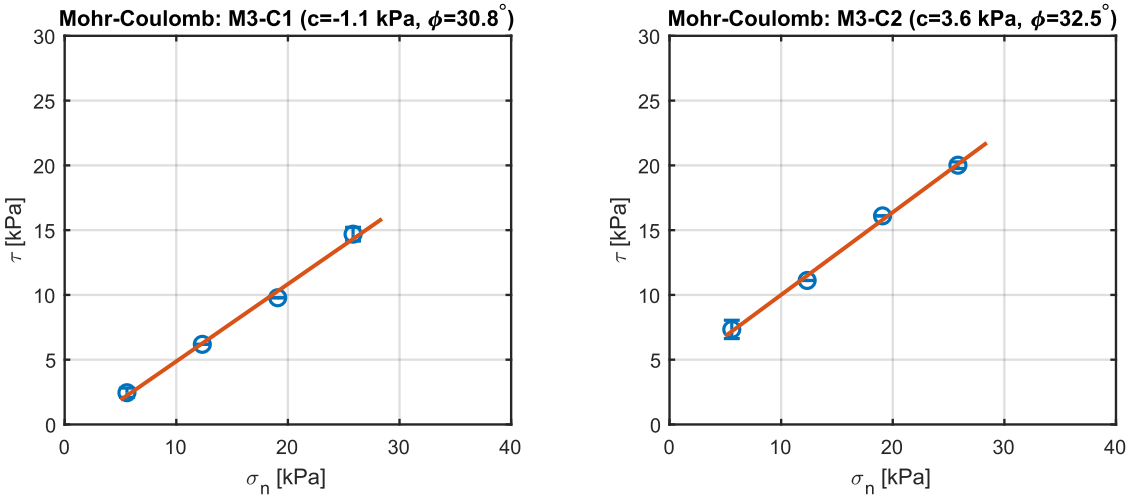

Figure 25. Individual Mohr-Coloumb plots for each individual material and condition.

5.2 Oedometer Results

The evolution of the mechanical response under cyclic oedometric loading for the three materials is collectively illustrated in Figure 26 - Figure 28. As shown, the stress–strain curves exhibit a progressive rightward shift with increasing cycle number, indicating continuous accumulation of permanent strain, while the increasing slope of the loading branches reflects gradual stiffening of the granular assembly. This behaviour is quantified in Figure 27, where the accumulated permanent strain increases rapidly during the initial cycles, followed by a diminishing rate of accumulation as the material approaches a more stable packing configuration. Among the materials, M1 displays the largest permanent strain, suggesting more pronounced particle rearrangement and a looser initial packing, whereas M2 and M3.2 exhibit more restrained deformation.

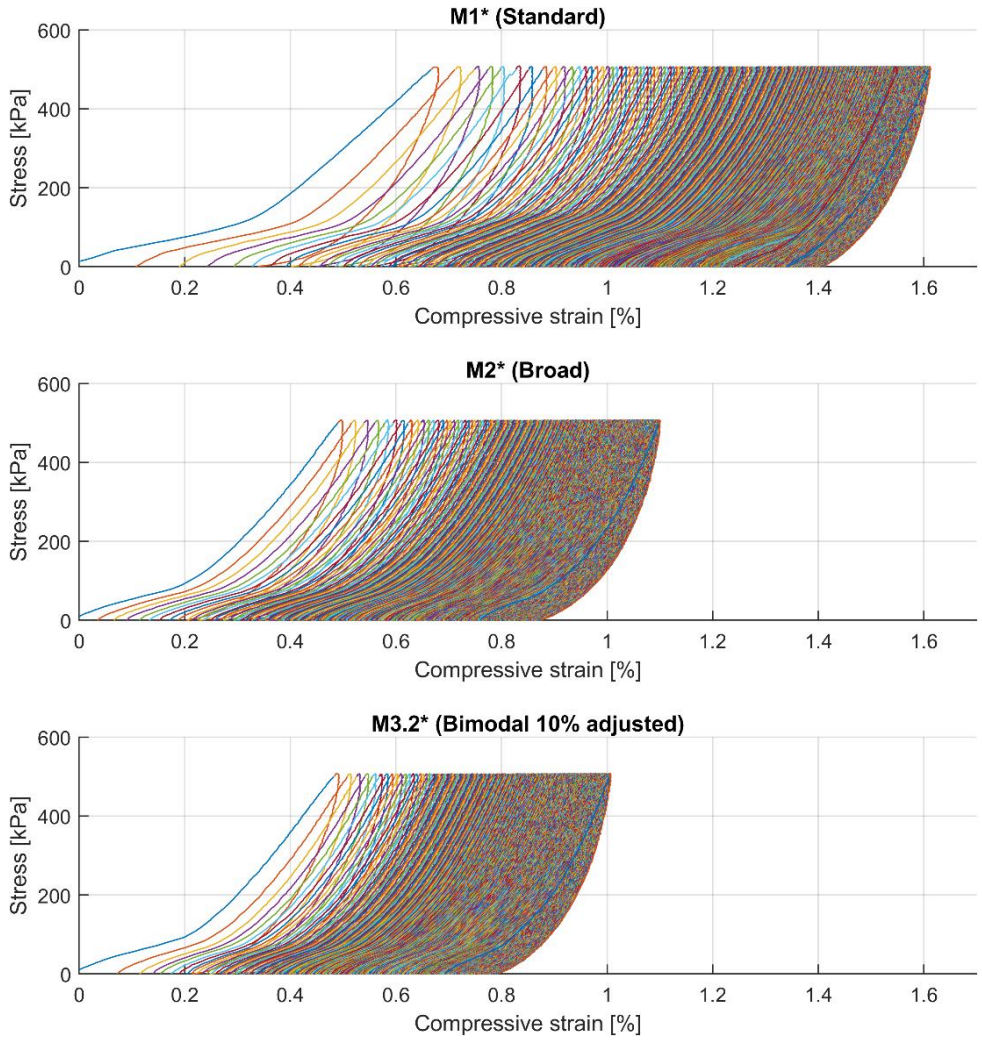

Figure 26. Cyclic oedometric stress–strain response for scaled materials M1, M2*, and M3.2* response.*

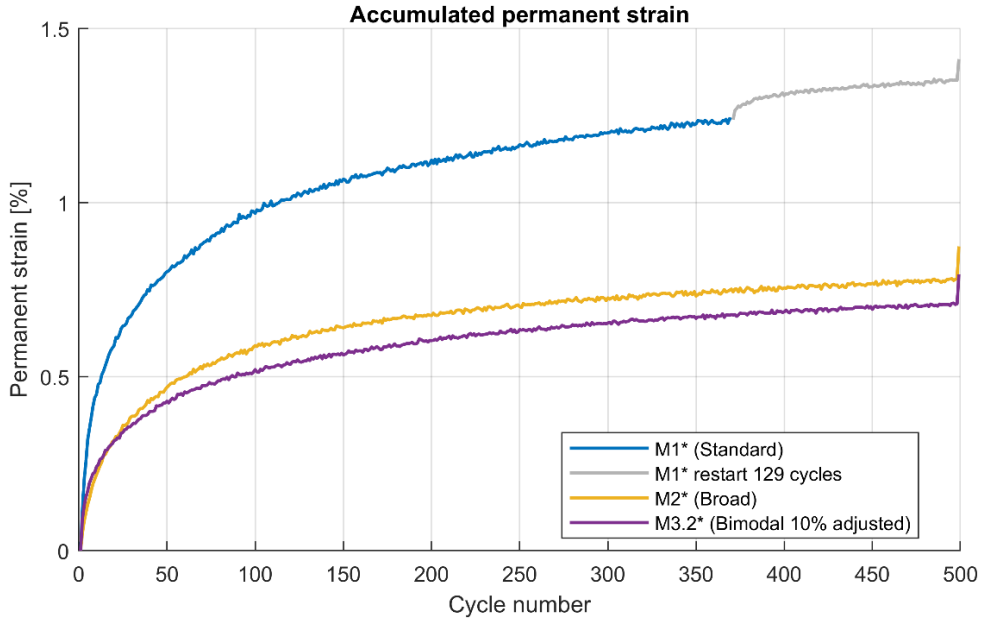

Figure 27. Accumulated permanent strain as a function of cycle number for materials M1, M2, and M3.2 during cyclic oedometric loading.

The corresponding evolution of stiffness is shown in Figure 28, where all materials demonstrate a clear increase in cyclic oedometric stiffness with cycle number, approaching a quasi-stabilized level after approximately 200–300 cycles. This stiffening trend is consistent with the densification observed in Figures 6 and 7, as increased contact density and improved force chain structure enhance the load-bearing capacity of the assembly. Notably, M3.2 exhibits a relatively high initial stiffness and a smooth evolution, while M2 shows a lower overall stiffness level. The apparent increase in stiffness for M1 at later cycles should be interpreted with caution, as it coincides with the transition between data files. Overall, the combined results highlight the strong influence of particle size distribution on both deformation accumulation and stiffness evolution under cyclic loading.

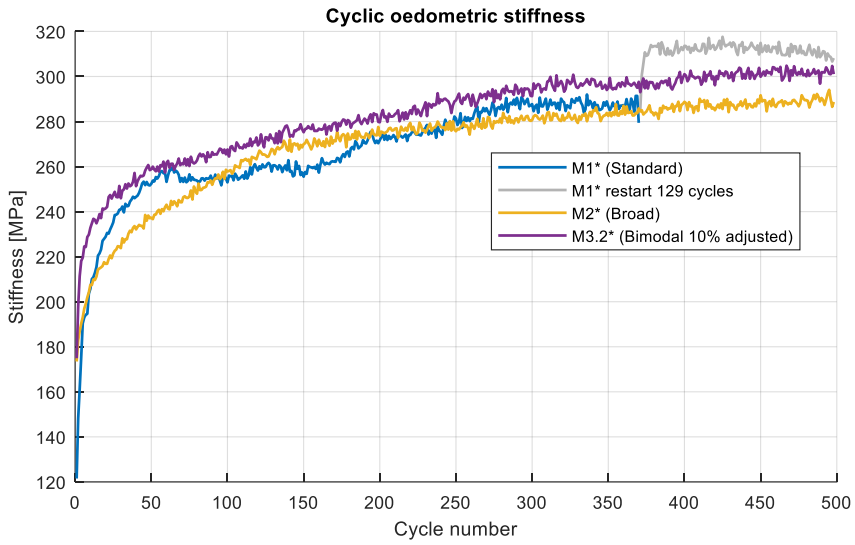

Figure 28. Cyclic oedometric stiffness as a function of cycle number for materials M1, M2, and M3.2, showing progressive stiffening and approach toward a stabilized response with increasing loading cycles.

5.2.1 Particle Size Distribution and Breakage Indices

The particle size distribution (PSD) of the ballast materials is described using both the cumulative passing distribution $Q_3(d)$and the frequency distribution q_3, where q_3 represents the mass fraction within each size interval and Q_3 the cumulative fraction passing a given particle size d.

The evolution of the particle size distributions due to cyclic loading is illustrated in Figure 29–Figure 32. The cumulative distributions (Figure 29) show a systematic upward shift for all materials in the intermediate size range, indicating an overall redistribution of mass toward smaller particle sizes. This effect is most pronounced for M2, which exhibits a noticeably steeper initial grading and correspondingly larger changes after testing.

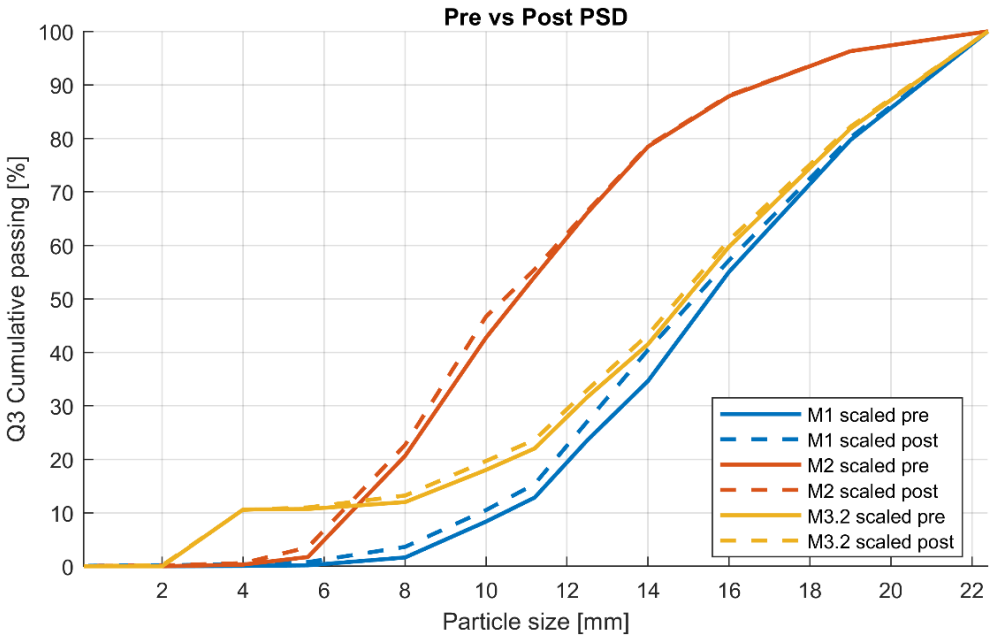

Figure 29. Cumulative particle size distributions Q3 for materials M1, M2, and M3.2 before and after cyclic oedometric loading.

The frequency distributions (Figure 30) provide a more detailed view of this redistribution. For all materials, a reduction in the coarser fractions is observed, accompanied by an increase in intermediate and fine fractions. This trend is particularly evident for M1, where substantial reductions occur in the largest size classes, indicating significant particle breakage of coarse particles.

The generation of fines (Figure 31) further highlights differences between the materials. M3.2 exhibits the highest accumulation of material in the 1–2 mm range, suggesting that the bimodal grading promotes fragmentation into this size class. In contrast, M1 and M2 show a more distributed fines production across the full sub-2 mm range, with relatively higher fractions in the smallest size classes.

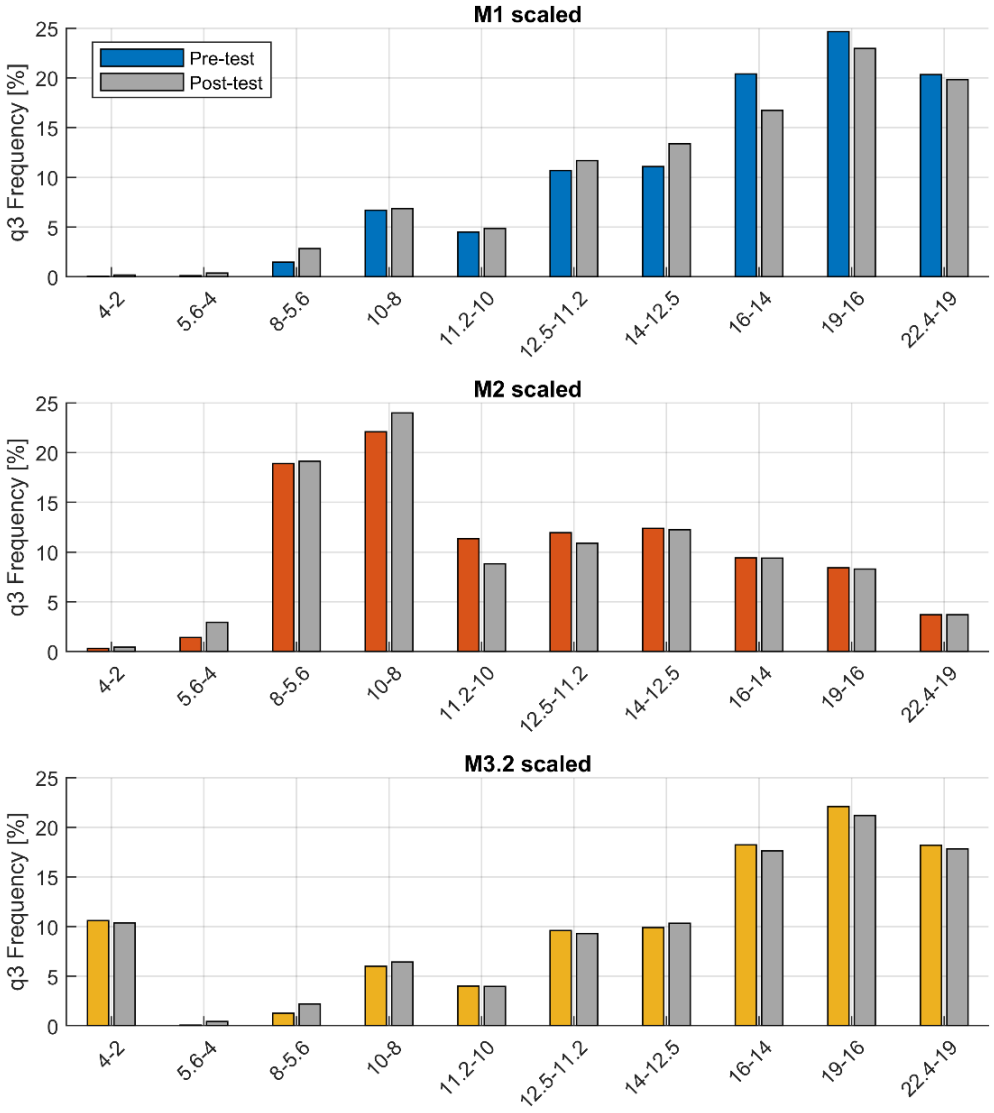

Figure 30. Frequency distributions q3 for materials M1, M2, and M3.2, showing mass fractions within each size interval before and after cyclic loading.

The redistribution of material is summarized in Figure 32 through the change in frequency distribution, Δq3. Positive values in the smaller size classes and corresponding negative values in the coarse fractions confirm that particle breakage is the governing mechanism. The magnitude and location of these changes differ between the materials, with M1 showing the most pronounced loss of coarse particles, while M2 and M3.2 exhibit more localized redistribution toward intermediate sizes.

The results demonstrate that the initial particle size distribution has a strong influence on both the extent and the mode of breakage, affecting not only the total fines generation but also the specific size ranges into which material is redistributed.

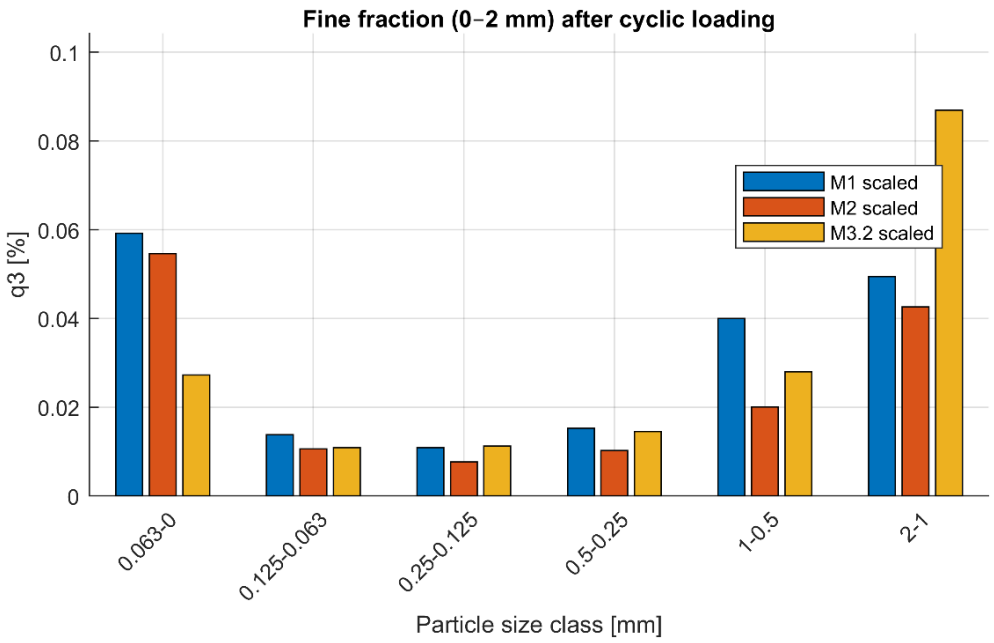

Figure 31. Frequency distribution of fine particles (0–2 mm) after cyclic loading for materials M1, M2, and M3.2.

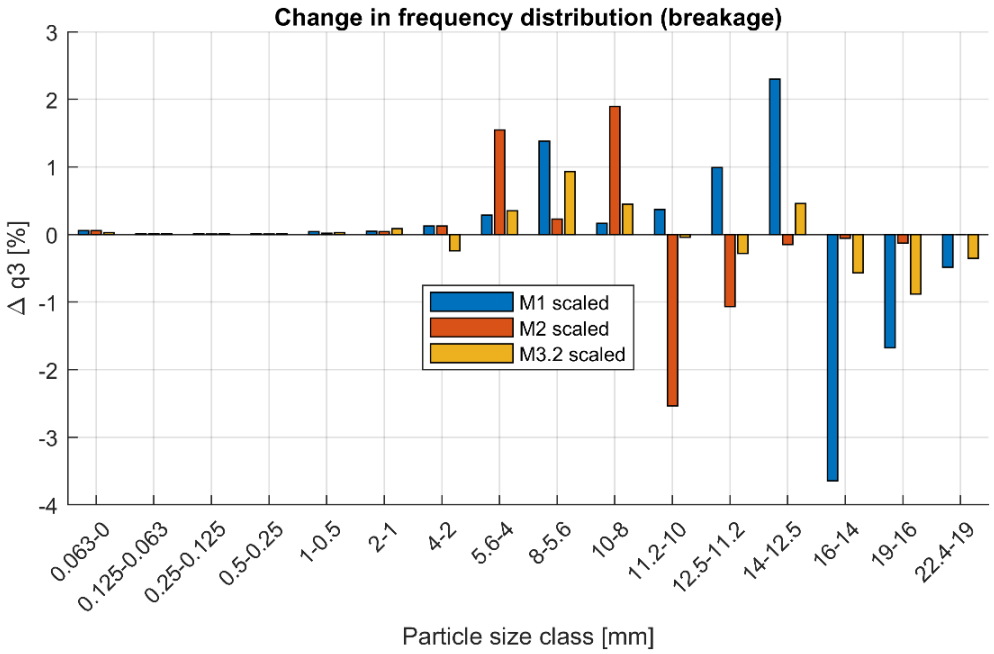

Figure 32. Change in frequency distribution Δq3 for materials M1, M2, and M3.2, highlighting redistribution of material across size classes due to particle breakage.

To quantify degradation due to cyclic loading, three complementary breakage measures were employed.

5.2.2 Absolute cumulative distribution change

The overall change in the PSD was first evaluated using the absolute difference in cumulative distributions,

$$B_Q = \sum_i | Q_{3,\text{post},i} - Q_{3,\text{pre},i} |$$

where $Q_{3,\text{pre},i}$and $Q_{3,\text{post},i}$denote the cumulative passing fractions before and after testing, respectively. This index provides a global measure of the redistribution of material across the entire size range, independent of the direction of change.

5.2.3 Marsal breakage index

The Marsal breakage index quantifies the generation of material in size classes that increase during testing, and is defined as

$$B_M = \sum_i \max\left(q_{3,\text{post},i} - q_{3,\text{pre},i}, 0\right)$$

This formulation considers only positive increments in the frequency distribution, thereby capturing the formation of new fragments due to particle breakage. The index is typically expressed as a percentage.

5.2.4 Fines generation

To specifically assess the production of fine material, the cumulative fraction of particles smaller than 2 mm was evaluated before and after testing,

$$F_{<2\,\text{mm}} = \sum_{d_i<2\,\text{mm}} q_{3,i}$$

and the total fines generation is given by

$$\Delta F_{<2\,\text{mm}} = F_{\text{post},<2\,\text{mm}} - F_{\text{pre},<2\,\text{mm}}$$

In addition to the incremental fines generation, the total fines content after testing, $F_{\text{post},<2\,\text{mm}}$, is reported as an indicator of the final state of material degradation.

5.2.5 Interpretation of indices

The selected indices provide complementary perspectives on ballast degradation:

- B_Q reflects the overall redistribution of material across the PSD
- B_M captures the generation of new fragments due to particle breakage
- $F_{<2\,\text{mm}}$ isolates the formation of fines, which is particularly relevant for ballast performance and fouling

Together, these measures enable a consistent and physically interpretable assessment of breakage behaviour across different particle size distributions. As shown in Table 6, material M1 exhibits the highest values for both the cumulative redistribution index B_Q and the Marsal breakage index B_M, indicating a more extensive overall rearrangement of the particle size distribution and a higher degree of fragment generation compared to the other materials. In contrast, M2 and M3.2 show lower values of $B_Q$and B_M, suggesting a reduced extent of particle breakage and redistribution.

Despite this, the fines content $F_{<2\,\text{mm}}$ does not follow the same trend, with M3.2 exhibiting a relatively high fines content compared to M2. This implies that while the

total amount of breakage in M3.2 is lower, a larger proportion of the fragmentation results in fine particles. This behaviour is consistent with the bimodal nature of M3.2, where the presence of smaller particles may promote localized crushing and the generation of fines rather than broad redistribution across multiple size classes.

Table 6. Summary of breakage indices for materials M1, M2, and M3.2 after cyclic oedometric loading, including the cumulative distribution change B_Q, the Marsal breakage index B_M (expressed in percent), and the final fines content below 2 mm, $F_{<2\,mm}$.

Material	B_Q	B_M	$F_{<2\,mm}$
M1	0.2017	5.807	0.1886
M2	0.1064	3.938	0.1456
M3.2	0.1004	2.365	0.1789

The results indicate that the particle size distribution has a significant influence on the fragmentation behaviour, affecting both the magnitude of breakage and the manner in which material is redistributed, distinguishing between widespread fragmentation and more targeted fines production.

6 Numerical Results

6.1 Sleeper Push Simulation

In order to calibrate the sleeper push simulation, a full factorial DOE (Design of Experiments) is performed for the parameters which are believed to have the largest influence on the results. In this project, the chosen variables are: particle-sleeper friction, particle-sleeper restitution and particle-particle friction during bed initialisation. The particle-sleeper friction and restitution are the main variables that govern the interaction between the sleeper and particle bed, while the particle-particle friction during bed initialization is directly tied to the degree of compaction of the ballast bed. This friction is only used during bed initialization to reach a certain packing density, and not for the remainder of the sleeper push simulation. A low, middle and high value is chosen for each of these parameters, which are seen in Table 7.

Table 7: DOE variable upper and lower bound ranges

Variable	Low	Middle	High
Particle-sleeper friction	0.1	0.5	0.9
Particle-sleeper restitution	0.1	0.5	0.9
Particle-particle friction	0.01	0.255	0.5

A Full factorial DOE with three variables gives 8 simulations. These along with two simulations at the middle of all parameters give a total of 10 simulations. These simulations and all parameters used are seen in Table 8.

Table 8: All DOE simulation settings

Simulation name	Particle-sleeper friction	Particle-sleeper restitution	Particle-particle friction
Sim1	0.1	0.1	0.01
Sim2	0.1	0.1	0.5
Sim3	0.1	0.9	0.01
Sim4	0.1	0.9	0.5
Sim5	0.9	0.1	0.01
Sim6	0.9	0.1	0.5
Sim7	0.9	0.9	0.01
Sim8	0.9	0.9	0.05
Sim9	0.5	0.5	0.255
Sim10	0.5	0.5	0.255

From these simulations, the following force-displacement plot is given in Figure 33, where the solid lines are the force-displacement data while the dashed lines are the corresponding asymptotic forces.

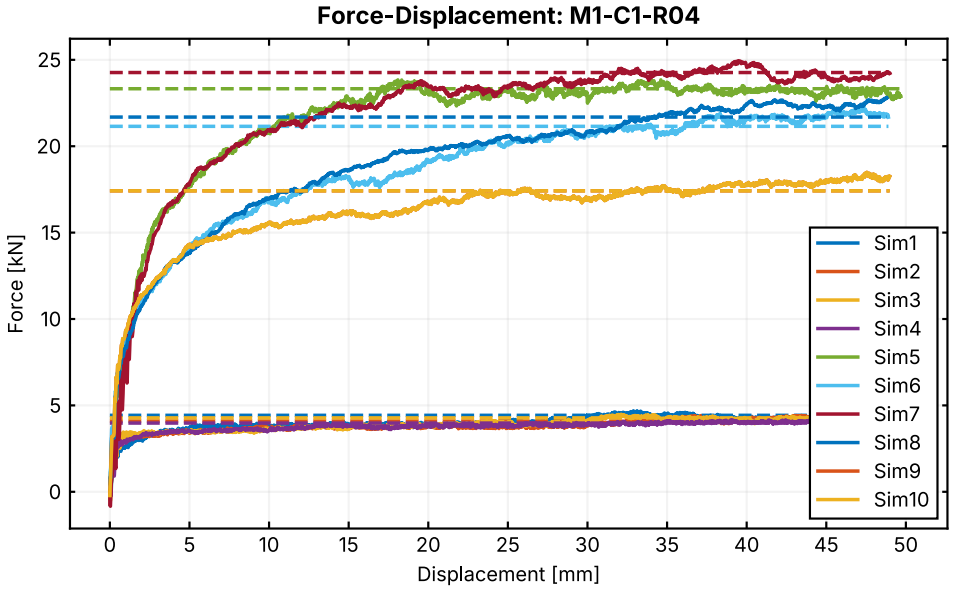

Figure 33: Force-displacement plot of DOE study

From this plot it can be seen that a high particle-sleeper friction along with a low initial particle-particle friction leads to a high asymptotic force. The settlement of the sleeper push rig from all the simulations can be seen in Figure 34.

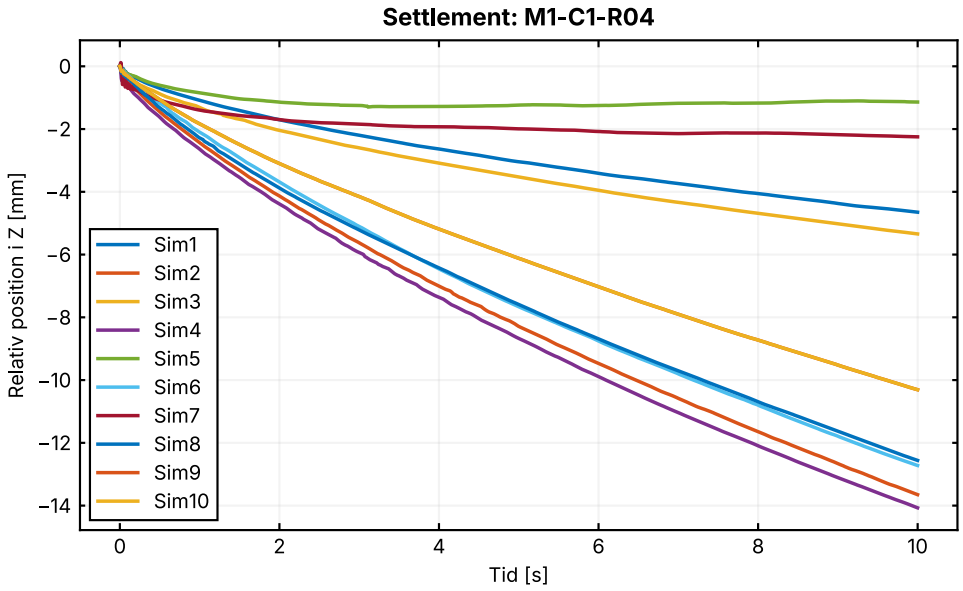

Figure 34: Sleeper vertical settlement plot of for the simulations performed in the DOE study.

In this figure, a high particle-sleeper friction along with a low initial particle-particle friction gives less settlement. Further, the figure indicates that a lower particle-sleeper restitution yields slightly less settlement.

6.2 Oedometer Simulation

Figure 35 presents the simulated stress–strain response of materials M1 and M2 (scaled particle size distribution) subjected to cyclic trapezoid loading from the oedometer simulation for seven cycles. For both materials, the strain response exhibits a clear progressive accumulation of permanent strain with increasing cycle number. Because only the first seven cycles are simulated, the observed behavior is dominated by early-stage particle rearrangement and particle packing. In agreement with the experimental trends reported in Section 5.2, M1 develops the largest strain, while M2 shows a more limited deformation over the same number of cycles. However, the simulated strains are larger than the experimentally measured strains. An explanation is the initial specimen preparation and packing state. In the simulations, the initial packing does not reproduce the comparatively flatter particle surface bed achieved experimentally, which can lead to a more initial packing in the simulations.

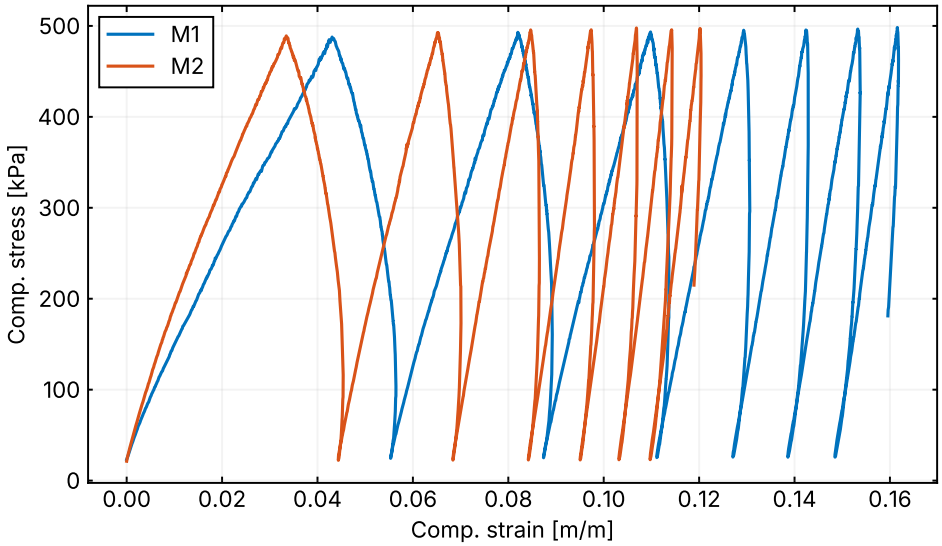

Figure 35: Stress-strain curves for two of the materials M1 and M2 with a scaled particle size distribution.

Figure 36 shows the corresponding evolution of bed stiffness over the loading cycles. In line with the experimental response, M2 exhibits a higher bed stiffness than M1 over the investigated cycles. This indicates that M2 forms a more stable particle bed, which is consistent with its lower strain accumulation.

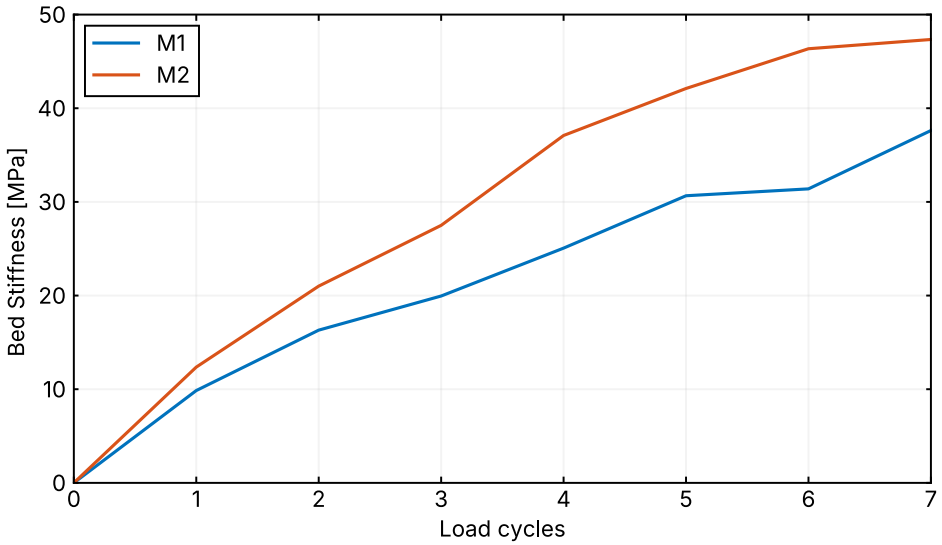

Figure 36: Bed stiffness for two of the materials M1 and M2 with a scaled particle size distribution.

The particle force distributions at the first stress peak are presented in Figure 37–Figure 39. Figure 37 shows that M2 contains a larger number of particles than M1, which is expected from its higher proportion of smaller particles (see Figure 30). As the applied load is distributed over a larger particle population, the force carried by individual particles is generally lower for M2.

This is further supported by the frequency and cumulative force distributions in Figure 38 and Figure 39. Compared with M2, M1 exhibits a broader force distribution with a more pronounced tail toward higher force norms, indicating more localized load transfer through highly loaded contacts. This provides a plausible particle-scale explanation for the experimental observations, where M1 showed larger permanent strain and more extensive breakage, while M2 exhibited lower deformation and higher stiffness.

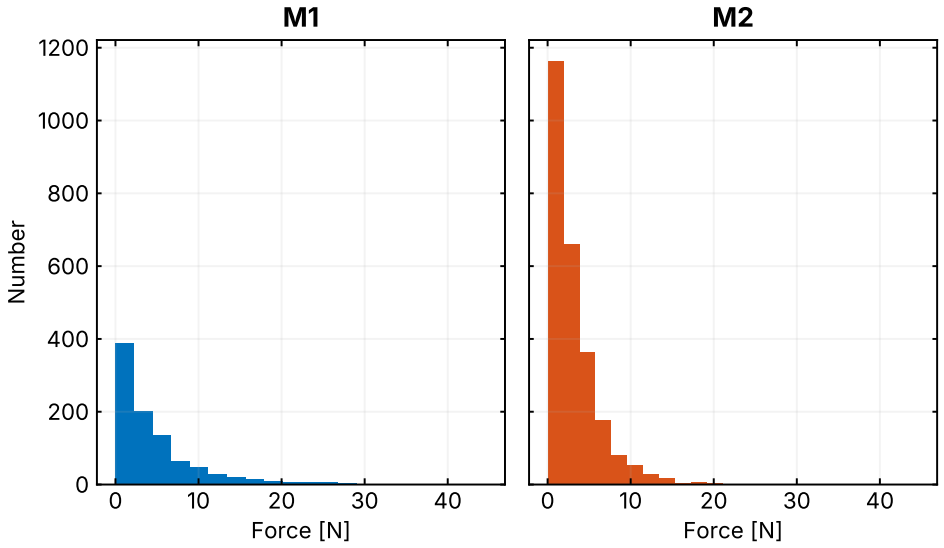

Figure 37: Number of particles against force norm distribution for two of the materials M1 and M2 with a scaled particle size distribution.

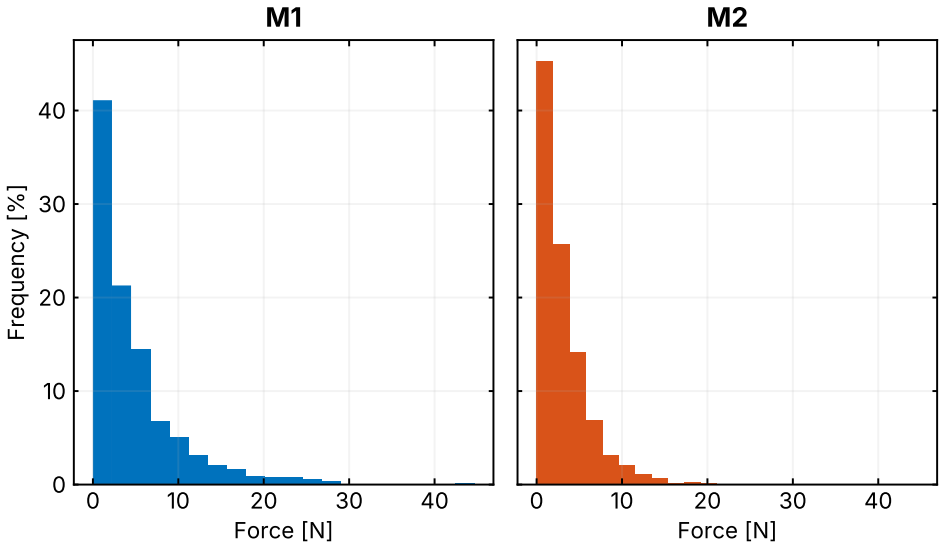

Figure 38: Frequency against force norm distribution for two of the materials M1 and M2 with a scaled particle size distribution.

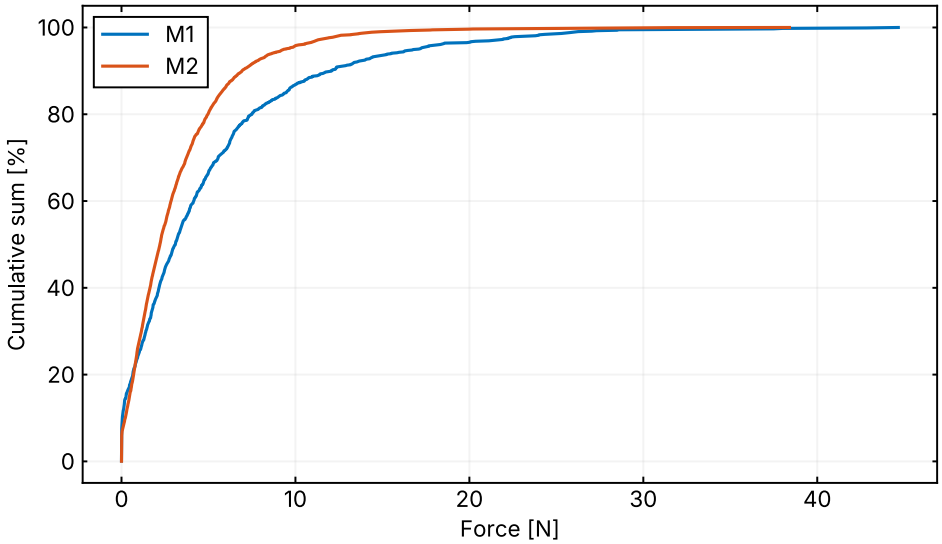

Figure 39: Cumulative sum against force norm distribution for two of the materials M1 and M2 with a scaled particle size distribution.

7 Comparison Between Experiments and Simulations

7.1 Force Response Comparison

Based on the DOE analysis, a single parameter set was selected to represent a reasonable compromise between force level and settlement. The selected parameters correspond to high particle–sleeper friction, low restitution, and low initial particle–particle friction, which were identified in the DOE as governing increased asymptotic force and reduced settlement.

Using this parameter set, additional simulations were performed for each material. The comparison with the corresponding experiments is shown in Figure 40–Figure 42. The simulations reproduce the asymptotic force level reasonably well for M1 and M2, although the force level for M2 is slightly underestimated. The overall shape of the force–displacement response is also captured, with similar rates of force development for M2 and M3, while M1 shows a somewhat slower force build-up in the simulations.

The corresponding settlement results are presented in Figure 43.

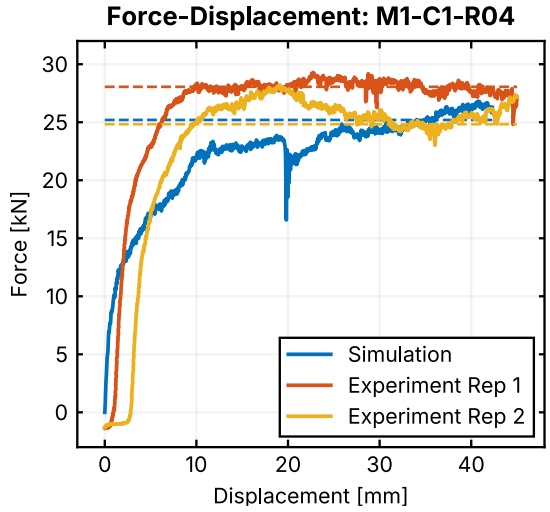

Figure 40: Force-displacement comparison of simulation and experiments for M1.

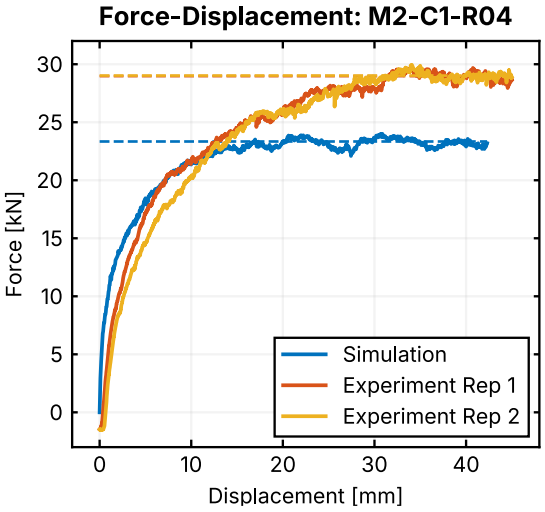

Figure 41: Force-displacement comparison of simulation and experiments for M2.

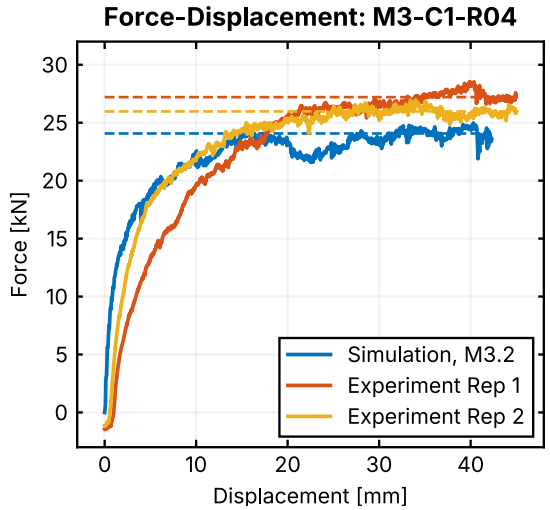

Figure 42: Force-displacement comparison of simulation and experiments for M1.

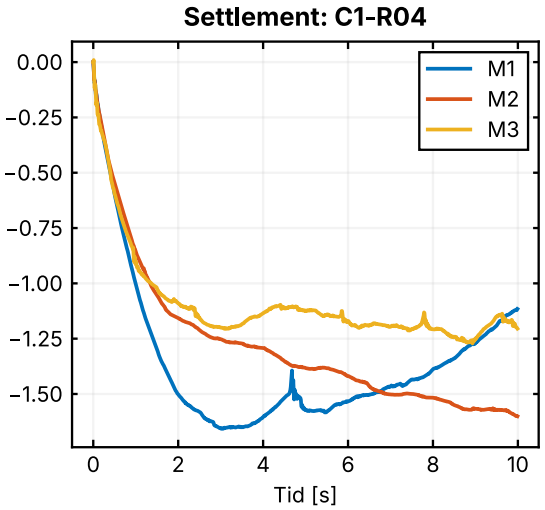

Figure 43: Settlement of sleeper push rig from simulations.

7.2 Comparison of Oedometer Simulations and Experiments

The oedometer simulations were completed for M1 and M2, while M3.2 was not included in the comparison. The discussion therefore focuses on qualitative trends between simulation and experiments.

The simulated stress–strain response (Figure 35) reflects the same material ranking as observed experimentally, with M1 showing a larger accumulation of permanent strain and M2 a more limited deformation. The absolute strain levels are higher in the simulations, which is attributed to differences in initial packing, but the relative behavior is consistent. A similar trend is observed for bed stiffness (Figure 36), where M2 remains stiffer than M1 across the loading cycles. This indicates that the

simulations capture the influence of particle size distribution on the stability of the particle skeleton.

The particle force distributions (Figure 37–Figure 39) provide a mechanistic explanation for these differences. M2 shows a higher proportion of particles carrying lower forces, while M1 exhibits a broader distribution with more highly loaded contacts. This suggests more localized load transfer in M1, which is consistent with the higher breakage and larger strain observed experimentally, whereas the more distributed force network in M2 aligns with its lower breakage and higher stiffness.

8 Conclusions

The following conclusions can be drawn from the present study:

- Particle size distribution influences both deformation and fragmentation behaviour of railway ballast, confirming that PSD is a relevant design parameter for ballast performance.
- In the cyclic oedometer tests, the standard ballast M1 exhibited the largest permanent deformation, the highest overall redistribution of material, and the highest breakage index. The broader grading M2 and the adjusted bi modal grading M3.2 showed lower overall breakage.
- The bi modal material M3.2 showed relatively high fines content despite lower total breakage, indicating that different PSDs may lead to different fragmentation modes rather than only different fragmentation magnitudes.
- In the sleeper push tests, vertical load and lateral confinement had a stronger influence on mobilized resistance than the tested PSD variations. Confinement mainly increased the apparent cohesion, while the friction angle remained relatively similar across materials.
- The DEM simulations reproduced the main qualitative trends observed experimentally, including the force-displacement response in the sleeper push test and the relative deformation and stiffness ranking between M1 and M2 in the oedometer simulations.
- The DEM results indicate that differences in force transmission provide a plausible particle scale explanation for the experimental trends: M1 develops more localized highly loaded contacts, while M2 distributes load over a larger particle population.
- The present simulations provide a useful baseline for comparative DEM analysis of ballast PSDs, but the absence of particle breakage limits direct prediction of degradation and fines generation.
- The generated experimental and numerical dataset provides a valuable basis for future calibration, validation, and systematic exploration of ballast grading and particle shape effects.

9 Recommendations for Future Work

The present study represents an initial evaluation of alternative ballast particle size distributions and is therefore limited in scope. The results indicate that particle size distribution has a clear influence on both mechanical response and fragmentation behaviour, but the observed trends also highlight the need for a more systematic exploration of the governing parameters.

The current experimental and numerical framework enables such an extension. With established test methodologies and corresponding DEM models for both oedometer and sleeper push configurations, the work provides a basis for expanding the analysis toward a more comprehensive representation of the full test program, allowing closer alignment between experimental conditions and numerical evaluation.

The available modelling capability further allows efficient exploration of a broader design space than is feasible experimentally. This includes systematic variation of grading width, bimodality, characteristic size ranges, and particle shape distributions, with the possibility to assess their influence from multiple perspectives, including mechanical performance, degradation behaviour, and production-related considerations.

At the same time, the study indicates clear benefits of complementing the current test configurations with larger-scale experimental setups, enabling evaluation at more representative particle sizes and stress conditions. Such extensions would strengthen the link between laboratory-scale observations and field-relevant behaviour, particularly with respect to deformation mechanisms and breakage processes.

While the DEM models capture the dominant mechanical trends, further refinement is required to improve quantitative agreement, especially in the oedometer response. In particular, the inclusion of particle breakage and enhanced representation of initial packing conditions would allow a more complete description of long-term ballast behaviour.

10 References

Berggren, E. (2009). Railway Track Stiffness: Dynamic Measurements and Evaluation for Efficient Maintenance [Doctoral thesis, comprehensive summary, KTH]. In *Trita-AVE* (2009:17). DiVA. http://urn.kb.se/resolve?urn=urn:nbn:se:kth:diva-10360

Dehlbom, B., Håkansson, S., & Berggren, E. (2018). *Förbättring av bärighet hos befintliga järnvägsanläggningar* (Issue 1.1-1604–0296).

Göransson, M. (2018). *Kritiska egenskaper hos bergmaterial och alternativa material* (Issue Rapport nr 2014-04247).

Indraratna B., Ionescu D., & Christie H. D. (1998). Shear Behavior of Railway Ballast Based on Large-Scale Triaxial Tests. *Journal of Geotechnical and Geoenvironmental Engineering*, *124*(5), 439–449. https://doi.org/10.1061/(ASCE)1090-0241(1998)124:5(439)

Indraratna, B., Sun, Y., & Nimbalkar, S. (2016). Laboratory Assessment of the Role of Particle Size Distribution on the Deformation and Degradation of Ballast under Cyclic Loading. *Journal of Geotechnical and Geoenvironmental Engineering*, *142*(7), 04016016–04016016. https://doi.org/10.1061/(ASCE)GT.1943-5606.0001463

Lundqvist, A., & Dahlberg, T. (2005). Railway track stiffness variation—Consequences and countermeasures. *19th IAVSD Symposium of Dynamics of Vehicles on Roads and Tracks, 2005*. DiVA. 19th IAVSD Symposium of Dynamics of Vehicles on Roads and Tracks, Milano, August 29-Seprember 2, 2005. http://urn.kb.se/resolve?urn=urn:nbn:se:liu:diva-41855

Rosa, A. F., Aragão, F. T. S., & da Motta, L. M. G. (2021). Effects of particle size distribution and lithology on the resistance to breakage of ballast materials. *Construction and Building Materials*, *267*, 121015–121015. https://doi.org/10.1016/j.conbuildmat.2020.121015

SIS. (2003). *SS-EN 13450—Aggregates for railway ballast*. (SS-EN 13450).

Trafikverket. (2015). *BVS 585.52—Makadamballast för järnväg* (Version 1.0). Trafikverket.

Trafikverket. (2020). *TRVINFRA-00019 Banöverbyggnad Makadamballast* (Version 1.0) [Krav infrastrukturregelverk]. Trafikverkets infrastrukturregelverk.